Deformation of Ne isotopes in the region of the island of inversion

Takenori Sumi,[1] Kosho Minomo,[1] Shingo Tagami,[1] Masaaki Kimura,[2] Takuma Matsumoto,[1] Kazuyuki Ogata,[3]
Yoshifumi R. Shimizu,[1] and Masanobu Yahiro[1]

[1]*Department of Physics, Kyushu University, Fukuoka 812-8581, Japan*
[2]*Creative Research Institution (CRIS), Hokkaido University, Sapporo 001-0021, Japan*
[3]*Research Center of Nuclear Physics (RCNP), Osaka University, Ibaraki 567-0047, Japan*
(Received 17 November 2011; revised manuscript received 16 April 2012; published 19 June 2012)

Deformations of Ne isotopes in the island of inversion are determined by the folding model description of the interaction cross sections measured for $^{28-32}$Ne isotopes incident on a ^{12}C target at 240 MeV/nucleon, using the Melbourne g-matrix interaction and the nuclear densities calculated by antisymmetrized molecular dynamics (AMD). The double folding model with the AMD density well reproduces the measured interaction cross sections, if the tail correction is made to the AMD density for ^{31}Ne. The quadrupole deformation determined is around 0.4 in the island of inversion and ^{31}Ne is a halo nucleus with large deformation. We propose the Woods-Saxon model with the AMD deformation and a suitably chosen parametrization set as an approximate but simple method to reproduce the AMD density with the tail correction. The angular momentum projection is essential to obtain the large deformation in the island of inversion. Effects of the pairing correlation are investigated.

I. INTRODUCTION

Exploring the so-called "island of inversion" is one of the most important current subjects in nuclear physics. The term "island of inversion" was first introduced by Warburton [1] to the region of unstable nuclei from ^{30}Ne to ^{34}Mg. In the region, the low excitation energies and the large $B(E2)$ values of the first excited states suggest strong deformations [2–6]. This indicates that the $N = 20$ magic number is no longer valid. This novel quantum property has triggered extensive experimental and theoretical studies on the island of inversion.

Another important progress of research on unstable nuclei is the discovery of halo nucleus [7–9]. Very recently, the interaction cross section $\sigma_{\rm I}$ was measured by Takechi *et al.* [10] for the scattering of $^{28-32}$Ne at 240 MeV/nucleon and the cross section was found to be quite large for ^{31}Ne. A halo structure of ^{31}Ne was reported by Nakamura *et al.* [11] through the measurement of the one-neutron removal reaction. This is the heaviest halo nucleus in the present stage suggested experimentally. The nucleus resides in the island of inversion. The interaction cross section and the nucleon-removal cross section with radioactive beams are thus important experimental tools of exploring unstable nuclei [7–12]. For the scattering of unstable nuclei at intermediate energies, $\sigma_{\rm I}$ agrees with the reaction cross section $\sigma_{\rm R}$ exactly or nearly, since projectile excitations to its discrete excited states do not exist or small even if they exist. This is discussed in this paper.

A useful theoretical tool of analyzing measured reaction cross sections is the microscopic optical potential constructed by the double-folding model (DFM) with the g-matrix effective nucleon-nucleon interaction [13–22], when the projectile breakup is weak. For the nucleon-nucleus scattering, the single-folding model with the Melbourne g-matrix well reproduces the measured $\sigma_{\rm R}$ and elastic cross sections systematically [20]. For the scattering of ^{31}Ne from a ^{12}C target at 240 MeV/nucleon, the breakup cross section is about 1% of

$\sigma_{\rm R}$ [23]. This indicates that the DFM is reliable for all the scattering of $^{20-32}$Ne, since ^{31}Ne is the most weakly bound system among them.

In the DFM, the microscopic optical potential is constructed by folding the g-matrix with projectile and target densities. The density profile changes, if it is deformed. The elongation makes the surface diffuseness and the root-mean-square (rms) radius effectively larger and eventually enhances $\sigma_{\rm R}$. The amount of deformation is thus important. Nuclei in the island of inversion are spherical or only weakly deformed in Hartree-Fock (HF) and Hartree-Fock-Bogoliubov (HFB) calculations with the Skyrme and the Gogny interaction; see for example Refs. [24,25]. It is even pointed out that the observed large $B(E2; 2^+ \to 0^+)$ values can be understood as a large amplitude vibration around the spherical shape [26]. In such a situation, the additional correlations by the angular momentum projection (AMP) often lead to possible deformed shapes; see Ref. [27] for Ne isotopes.

Recently a systematic analysis was made by antisymmetrized molecular dynamics (AMD) with the Gogny-D1S interaction for both even- and odd-N nuclei in the island of inversion [28,29]. The AMP-AMD calculations, i.e., the AMD calculation with the AMP, yield large deformations. This is consistent with the result of AMP-HFB calculations [25,27]. A consistent picture of even and odd isotopes has been obtained by the AMP-AMD approach, where n-particle m-hole excitations of the Nilsson orbits play important roles to determine deformed configurations. Although it is difficult to distinguish the dynamic shape-fluctuation from the static deformation in these light mass nuclei, one may use the deformed shape suggested by the AMD calculation to see its effect on $\sigma_{\rm R}$. Very recently the Woods-Saxon mean-field model with the deformation obtained by the AMP-AMD calculation was applied to $^{28-32}$Ne and the DFM with the density of the mean-field model was successful in reproducing the data on $\sigma_{\rm R}$ in virtue of the large deformation [30].

In principle, one can calculate the double-folding potential directly by using the nucleon density calculated with AMD. The nucleon density is, however, inaccurate in the asymptotic region, since each nucleon is described by a Gaussian wave packet in AMD. Very lately we proposed a way of making a tail correction to the AMD density [31]. Although the calculation based on the resonating group method is quite time-consuming, it has been applied to ^{31}Ne [31] that is the most weakly bound system among $^{20-32}$Ne. The tail correction to $\sigma_{\rm R}$ is about 3% for ^{31}Ne. The DFM with the tail-corrected density reproduces the measured $\sigma_{\rm I}$ for ^{31}Ne, whereas the DFM without the tail correction underestimates the data considerably.

In this paper, we determine deformations of $^{20-32}$Ne systematically by using AMD. The theoretical prediction on the deformation is verified by analyzing the measured interaction cross sections for $^{20,28-32}$Ne with the DFM with the Melbourne g-matrix. In the DFM, the projectile density is constructed either (I) by the AMP-AMD calculation with the Gogny-D1S interaction or (II) by the Woods-Saxon model with the deformation obtained by the AMP-AMD calculation. Model I has no adjustable parameter, but the density is inaccurate in the asymptotic region. Model II provides the nucleon density with the proper asymptotic form, but the model includes potential parameters. As the potential parameter set, we use the parameter set recently proposed by Wyss [32]. This set is intended to reproduce the spectroscopic properties of high-spin states from light to heavy deformed nuclei, e.g., the quadrupole moments and the moments of inertia and at the same time the rms radii crucial for the present analysis.

Models I and II yield almost the same $\sigma_{\rm R}$ for $^{24-29}$Ne that have large one-neutron separation energies. Furthermore, this agreement is seen for ^{31}Ne, when the tail correction is made in Model I. This indicates that Model II is a handy way of simulating results of Model I with the tail correction. Model II is quite practical compared with Model I with the tail correction that requires time-consuming calculations. Model I with the tail correction and Model II reproduce the measured $\sigma_{\rm I}$ of $^{20,28-32}$Ne. Deformations of $^{28-32}$Ne are thus definitely determined through this analysis. This analysis also yields a reasonable prediction for deformations of $^{21-27}$Ne. We also confirm that ^{31}Ne is a halo nucleus with large deformation. Furthermore, we analyze the AMP effect and the pairing effect on $\sigma_{\rm R}$ by using Model II.

We describe the theoretical framework of the present analysis in Sec. II. Namely, we explain the DFM, AMD with the AMP and the Woods-Saxon mean-field model with the AMP. We also present a handy way of making a center-of-mass (c.m.) correction and show that the dynamical deformation effect and the reorientation effect are small. This indicates that $\sigma_{\rm I} \approx \sigma_{\rm R}$. Numerical results are shown in Sec. III. Section IV is devoted to summary.

II. THEORETICAL FRAMEWORK

A. Double folding model

We consider the scattering of a projectile (P) on a target (T). The scattering is described by the many-body Schrödinger equation with the realistic nucleon-nucleon interaction v_{ij},

$$\left(T_R + h_{\rm P} + h_{\rm T} + \sum_{i \in {\rm P}, j \in {\rm T}} v_{ij} - E \right) \Psi^{(+)} = 0 , \quad (1)$$

where E is the energy of the total system, T_R is the kinetic energy of relative motion between P and T, and $h_{\rm P}$ ($h_{\rm T}$) is the internal Hamiltonian of P (T). The multiple-scattering theory [33,34] for nucleon-nucleus scattering was extended to nucleus-nucleus scattering [35]. According to the theory, Eq. (1) is approximated into

$$\left(T_R + h_{\rm P} + h_{\rm T} + \sum_{i \in {\rm P}, j \in {\rm T}} \tau_{ij} - E \right) \hat{\Psi}^{(+)} = 0 , \quad (2)$$

where τ_{ij} is the effective nucleon-nucleon interaction in the nuclear medium. The Brueckner g-matrix has often been used as such τ_{ij} in many applications; see, for example, Refs. [13–22]. The g-matrix interaction includes the nuclear-medium effect, but not the effect of collective excitations induced by the surface vibration and the rotation of finite nucleus, since the interaction is evaluated in the nuclear matter.

In the scattering analyzed here, effects of the collective excitations and the projectile breakup are small, since the target is light and E is large; see Sec. II E for the collective excitation and Sec. III B for the projectile breakup. In this situation the DFM becomes reliable. In the model, the potential U consists of the direct part ($U^{\rm DR}$) and the exchange part ($U^{\rm EX}$) defined by [36,37]

$$U^{\rm DR}(\boldsymbol{R}) = \sum_{\mu,\nu} \int \rho_{\rm P}^{\mu}(\boldsymbol{r}_{\rm P}) \rho_{\rm T}^{\nu}(\boldsymbol{r}_{\rm T}) g_{\mu\nu}^{\rm DR}(s; \rho_{\mu\nu}) d\boldsymbol{r}_{\rm P} d\boldsymbol{r}_{\rm T}, \quad (3)$$

$$U^{\rm EX}(\boldsymbol{R}) = \sum_{\mu,\nu} \int \rho_{\rm P}^{\mu}(\boldsymbol{r}_{\rm P}, \boldsymbol{r}_{\rm P} - s) \rho_{\rm T}^{\nu}(\boldsymbol{r}_{\rm T}, \boldsymbol{r}_{\rm T} + s)$$
$$\times g_{\mu\nu}^{\rm EX}(s; \rho_{\mu\nu}) \exp[-i\boldsymbol{K}(\boldsymbol{R}) \cdot s/M] d\boldsymbol{r}_{\rm P} d\boldsymbol{r}_{\rm T}, \quad (4)$$

where $s = \boldsymbol{r}_{\rm P} - \boldsymbol{r}_{\rm T} + \boldsymbol{R}$ for the coordinate $\boldsymbol{R}$ between P and T. The coordinate $\boldsymbol{r}_{\rm P}$ ($\boldsymbol{r}_{\rm T}$) denotes the location for the interacting nucleon measured from the center of mass of the projectile (target). Each of μ and ν stands for the z-component of isospin; $1/2$ means neutron and $-1/2$ does proton. The original form of $U^{\rm EX}$ is a nonlocal function of $\boldsymbol{R}$, but it has been localized in Eq. (4) with the local semiclassical approximation [15] in which P is assumed to propagate as a plane wave with the local momentum $\hbar\boldsymbol{K}(\boldsymbol{R})$ within a short range of the nucleon-nucleon interaction, where $M = A A_{\rm T}/(A + A_{\rm T})$ for the mass number A ($A_{\rm T}$) of P (T). The validity of this localization is shown in Ref. [38].

The direct and exchange parts, $g_{\mu\nu}^{\rm DR}$ and $g_{\mu\nu}^{\rm EX}$, of the effective nucleon-nucleon interaction (g-matrix) are assumed to depend on the local density

$$\rho_{\mu\nu} = \rho_{\rm P}^{\mu}(\boldsymbol{r}_{\rm P} - s/2) + \rho_{\rm T}^{\nu}(\boldsymbol{r}_{\rm T} + s/2) \quad (5)$$

at the midpoint of the interacting nucleon pair. The direct and exchange parts are described by

$$
g_{\mu\nu}^{\mathrm{DR}}(s;\rho_{\mu\nu})
$$
$$
= \begin{cases} \frac{1}{4}\sum_S \hat{S}^2 g_{\mu\nu}^{S1}(s;\rho_{\mu\nu}); & \text{for} \quad \mu+\nu=\pm 1 \\ \frac{1}{8}\sum_{S,T} \hat{S}^2 g_{\mu\nu}^{ST}(s;\rho_{\mu\nu}); & \text{for} \quad \mu+\nu=0 \end{cases}, \quad (6)
$$

$$
g_{\mu\nu}^{\mathrm{EX}}(s;\rho_{\mu\nu})
$$
$$
= \begin{cases} \frac{1}{4}\sum_S (-1)^{S+1}\hat{S}^2 g_{\mu\nu}^{S1}(s;\rho_{\mu\nu}); & \text{for} \quad \mu+\nu=\pm 1 \\ \frac{1}{8}\sum_{S,T} (-1)^{S+T}\hat{S}^2 g_{\mu\nu}^{ST}(s;\rho_{\mu\nu}); & \text{for} \quad \mu+\nu=0 \end{cases}, \quad (7)
$$

where $\hat{S} = \sqrt{2S+1}$ and $g_{\mu\nu}^{ST}$ are the spin-isospin components of the g-matrix interaction. As for the g-matrix interaction, we take the Melbourne interaction [20] constructed from the Bonn-B nucleon-nucleon potential [39].

In the DFM, the total wave function with the total angular momentum J and its z-component M is described by

$$
\Psi_{JM}^{(+)} = \sum_L \left[\Phi_{\mathrm{P}}^I(\xi_{\mathrm{P}}) \otimes Y_L(\hat{\boldsymbol{R}}) \right]_{JM} \Phi_{\mathrm{T}}^0(\xi_{\mathrm{T}}) \chi_{LJ}^{(+)}(R)/R, \quad (8)
$$

where Φ_{P}^I (Φ_{T}^0) represents the ground state wave function of P (T) with spin I (0) as a function of the internal coordinate ξ_{P} (ξ_{T}). Here the target spin is assumed to be zero for simplicity. Inserting Eq. (8) into Eq. (2) and left-multiplying the resulting equation by $\langle [\Phi_{\mathrm{P}}^I(\xi_{\mathrm{P}}) \otimes Y_L(\hat{\boldsymbol{R}})]_{JM} \Phi_{\mathrm{T}}^0(\xi_{\mathrm{T}}) |$ lead to the coupled-channel equations,

$$
\left[-\frac{\hbar^2}{2\mu_R}\frac{d^2}{dR^2} + \frac{\hbar^2 L(L+1)}{2\mu_R R^2} + U_{LL}(R) - E_{\mathrm{in}} \right] \chi_{LJ}^{(+)}(R)
$$
$$
= -\sum_{L'\neq L} U_{LL'}(R)\chi_{L'J}^{(+)}(R), \quad (9)
$$

for the relative wave function $\chi_{LJ}^{(+)}$ with the relative angular momentum L. Here μ_R is the reduced mass between P and T, and the incident energy E_{in} is related to the total energy E as $E_{\mathrm{in}} = E - \epsilon_{\mathrm{P}}^0 - \epsilon_{\mathrm{T}}^0$ for the ground-state energies ϵ_{P}^0 and ϵ_{T}^0 of P and T, respectively. In actual calculations, the relativistic kinematics is taken for E_{in} and μ_R in Eq. (9). It yields about a 2% reduction of reaction cross sections at the present intermediate energies.

The coupling potentials $U_{LL'}$ are defined by

$$
U_{LL'}(R) = \sum_{mM_L, m'M_{L'}} (ImLM_L|JM)(Im'L'M_{L'}|JM)
$$
$$
\times \int d\Omega_R Y_{LM_L}^*(\Omega_R) U(\boldsymbol{R}) Y_{L'M_{L'}}(\Omega_R), \quad (10)
$$

where m (M_L) is the z-component of I (L). When the projectile spin I is not zero, the folding potential $U(\boldsymbol{R})$ is nonspherical in general. Effects of the nonspherical part of $U(\boldsymbol{R})$ on the elastic scattering are called the reorientation effect. If the nonspherical part of $U(\boldsymbol{R})$ is neglected, the $U_{LL'}$ become diagonal, i.e., $U_{LL'} = U_0(R)\delta_{LL'}$ for the spherical part $U_0(R)$ of $U(\boldsymbol{R})$. This approximation corresponds to the standard optical model for elastic scattering. As shown in Sec. II E, this is a really good

approximation for scattering at intermediate energies such as 240 MeV/nucleon. We then take this approximation in this paper.

B. AMD framework and inputs for the reaction calculations

The framework and the calculational procedure of AMD are common to those of Ref. [29], and the reader is directed to it for more detail. The Hamiltonian of AMD is obtained by

$$
H = T + \sum_{i<j} \bar{v}_{ij} - T_{\mathrm{c.m.}}. \quad (11)
$$

As an effective nucleon-nucleon interaction $\bar{v}_{ij}$, we take the Gogny-D1S interaction [40], where the Coulomb part of $\bar{v}_{ij}$ is approximated by a sum of 12 Gaussians. T and $T_{\mathrm{c.m.}}$ represent the kinetic energies of nucleons and center-of-mass motion, respectively.

The variational wave function is a parity-projected wave function and the intrinsic wave function is a Slater determinant of nucleon wave packets,

$$
\Phi^\pi = P^\pi \mathcal{A}\{\varphi_1, \varphi_2, ..., \varphi_A\}, \quad (12)
$$

where P^π is the parity projector. The nucleon wave packet φ_i is a direct product of spatial ϕ_i, spin χ_i and isospin ξ_i parts,

$$
\varphi_i = \phi_i(\boldsymbol{r})\chi_i\xi_i, \quad (13)
$$
$$
\phi_i(\boldsymbol{r}) = \prod_{\sigma=x,y,z} \left(\frac{2\nu_\sigma}{\pi}\right)^{1/4} \exp\left\{ -\nu_\sigma \left(r_\sigma - \frac{Z_{i\sigma}}{\sqrt{\nu_\sigma}} \right)^2 \right\}, \quad (14)
$$
$$
\chi_i = \alpha_{i,\uparrow}\chi_\uparrow + \alpha_{i,\downarrow}\chi_\downarrow, \quad \xi_i = p \text{ or } n, \quad (15)
$$

where the centroids $\boldsymbol{Z}_i$, the width ν_σ and the spin directions $\alpha_{i,\uparrow}$ and $\alpha_{i,\downarrow}$ of Gaussian wave packets are the parameters determined variationally as explained below. The center-of-mass wave function can be analytically separated from the variational wave function Eq. (12):

$$
\Phi^\pi = \Phi_{\mathrm{c.m.}}\Phi_{\mathrm{int}}, \quad (16)
$$
$$
\Phi_{\mathrm{c.m.}} = \prod_{\sigma=x,y,z} \left(\frac{2A\nu_\sigma}{\pi}\right)^{1/4}
$$
$$
\times \exp\left\{ -A\nu_\sigma \left(X_\sigma - \frac{Z_{\mathrm{c.m.},\sigma}}{\sqrt{A\nu_\sigma}} \right)^2 \right\}, \quad (17)
$$
$$
\boldsymbol{Z}_{\mathrm{c.m.}} = \frac{1}{\sqrt{A}}\sum_{i=1}^A \boldsymbol{Z}_i, \quad (18)
$$

where X represents the center-of-mass coordinate and $\boldsymbol{Z}_{\mathrm{c.m.}}$ defined by Eq. (18) can be set to zero without loss of generality. This is common to the AMP and calculations of the generator coordinate method (GCM), and hence all quantities used as inputs of reaction calculations are free from the spurious center-of-mass motion.

The parameters in Eq. (12) are determined by using the frictional cooling method to minimize the total energy under the constraint on the matter quadrupole deformation parameter

$\bar{\beta}$. Here the quadrupole deformation parameters are defined as

$$\frac{\langle x^2 \rangle^{1/2}}{[\langle x^2 \rangle \langle y^2 \rangle \langle z^2 \rangle]^{1/6}} = \exp\left[\sqrt{\frac{5}{4\pi}} \bar{\beta} \cos\left(\bar{\gamma} + \frac{2\pi}{3}\right)\right], \quad (19)$$

$$\frac{\langle y^2 \rangle^{1/2}}{[\langle x^2 \rangle \langle y^2 \rangle \langle z^2 \rangle]^{1/6}} = \exp\left[\sqrt{\frac{5}{4\pi}} \bar{\beta} \cos\left(\bar{\gamma} - \frac{2\pi}{3}\right)\right], \quad (20)$$

$$\frac{\langle z^2 \rangle^{1/2}}{[\langle x^2 \rangle \langle y^2 \rangle \langle z^2 \rangle]^{1/6}} = \exp\left[\sqrt{\frac{5}{4\pi}} \bar{\beta} \cos\bar{\gamma}\right]. \quad (21)$$

Here, $\langle x^2 \rangle$, $\langle y^2 \rangle$, and $\langle z^2 \rangle$ are calculated from Φ_{int} in the intrinsic frame that is so chosen to satisfy the relation $\langle x^2 \rangle \leqslant \langle y^2 \rangle \leqslant \langle z^2 \rangle$. The constraint is imposed on the value of $\bar{\beta}$ from 0 to 1.0 with the interval of 0.025. Since we do not make any assumption on the spatial symmetry of the wave function and do not impose any constraint on $\bar{\gamma}$, it has an optimal value for each given value of $\bar{\beta}$.

After the variation, we perform the AMP for each value of $\bar{\beta}$,

$$\Phi_{mK}^{I\pi}(\bar{\beta}) = P_{mK}^I \Phi_{\text{int}}^\pi(\bar{\beta}), \quad (22)$$

$$P_{mK}^I = \frac{2I+1}{8\pi^2} \int d\Omega D_{mK}^{I*}(\Omega) R(\Omega), \quad (23)$$

where $D_{mK}^I(\Omega)$ and $R(\Omega)$ are Wigner's D function and rotation operator, respectively. The integrals over three Euler angles Ω in Eq. (23) are performed numerically.

The AMD calculation is completed by performing GCM. The wave functions that have the same parity and angular momentum (I, m) are superposed as

$$\Phi_n^{Im\pi} = \sum_{K=-I}^I \sum_{\bar{\beta}} c_{nK}(\bar{\beta}) \Phi_{mK}^{I\pi}(\bar{\beta}). \quad (24)$$

In other words, K and $\bar{\beta}$ are the generator coordinates in this calculation. The coefficients $c_{nK}(\bar{\beta})$ are determined by solving the Hill-Wheeler equation:

$$\sum_{\bar{\beta}'K'} H_{KK'}(\bar{\beta}, \bar{\beta}') c_{nK'}(\bar{\beta}') = E_n \sum_{\bar{\beta}'K'} N_{KK'}(\bar{\beta}, \bar{\beta}') c_{nK'}(\bar{\beta}'), \quad (25)$$

$$\left\{ \begin{array}{c} N_{KK'}(\bar{\beta}, \bar{\beta}') \\ H_{KK'}(\bar{\beta}, \bar{\beta}') \end{array} \right\} = \langle \Phi_{mK}^{I\pi}(\bar{\beta}) | \left\{ \begin{array}{c} 1 \\ H \end{array} \right\} | \Phi_{mK'}^{I\pi}(\bar{\beta}') \rangle. \quad (26)$$

The ground state wave function $\Phi_{\text{g.s.}}^{Im\pi}$ obtained by this procedure is used in the discussion of Sec. III.

For the reaction calculation, two types of applications are performed. One is to use the deformation parameters $\bar{\beta}$ and $\bar{\gamma}$ as inputs of deformed Woods-Saxon potential. We assign the deformation of the AMD wave function by picking up a GCM basis wave function that has the maximum overlap with the ground state wave function, $|\langle \Phi_{\text{g.s.}}^{Im\pi} | \Phi_{mK}^{I\pi}(\bar{\beta}) \rangle|^2$, and taking $\bar{\beta}$ of the GCM basis function and the corresponding $\bar{\gamma}$. The other is the direct use of the nucleon density calculated from the ground state wave function as an input of the double-folding potential,

$$\rho_{ImIm'}(\mathbf{r}) = \langle \Phi_{\text{g.s.}}^{Im\pi} | \sum_i \delta(\mathbf{r}_i - \mathbf{X} - \mathbf{r}) | \Phi_{\text{g.s.}}^{Im'\pi} \rangle, \quad (27)$$

$$= \sum_{\lambda=0}^{2I} \rho_{II}^{(\lambda)}(r)(Im'\lambda\mu | Im) Y_{\lambda\mu}^*(\hat{r}), \quad (28)$$

where the summation of λ in Eq. (28) runs for even numbers. When only $\rho_{II}^{(\lambda=0)}$ is taken in the double-folding potential, the resultant folding potential becomes spherical. This approximation is often used as a standard manner in the DFM, since this reduces the coupled-channel equations (9) to a single-channel one. The validity of this approximation is shown in Sec. II E.

C. Woods-Saxon mean-field model

We also calculate the double-folding potential with the density calculated by the Woods-Saxon mean-field model. Sophisticated AMD calculation is a powerful tool but it costs much time to obtain reliable information. We then take the deformed Woods-Saxon model as an alternative approach and also for further investigation.

The deformed Woods-Saxon potential is composed of the central and spin-orbit parts, which have the following forms:

$$V_c(\mathbf{r}) = \frac{V_0}{1 + \exp[\text{dist}_\Sigma(\mathbf{r})/a]}, \quad (29)$$

$$V_{\text{so}}(\mathbf{r}) = \lambda_{\text{so}} \left(\frac{\hbar}{2m_{\text{red}}c}\right)^2 \nabla V_c(\mathbf{r}) \cdot \left(\boldsymbol{\sigma} \times \frac{1}{i}\nabla\right), \quad (30)$$

where $m_{\text{red}} = m(A-1)/A$ and $\text{dist}_\Sigma(\mathbf{r})$ represents a distance between a given point $\mathbf{r}$ and the deformed surface Σ specified by the radius,

$$R(\theta, \phi; \boldsymbol{\alpha}) = R_0 c_v(\boldsymbol{\alpha}) \left[1 + \sum_{\lambda\mu} \alpha_{\lambda\mu}^* Y_{\lambda\mu}(\theta, \phi)\right], \quad (31)$$

with the deformation parameters $\boldsymbol{\alpha} \equiv \{\alpha_{\lambda\mu}\}$. The constant $c_v(\boldsymbol{\alpha})$ is introduced to guarantee the volume conservation of nucleus. A set of deformation parameters used in the present work is $(\beta_2, \gamma, \beta_4)$ [41], which are related to $(\alpha_{2\mu}, \alpha_{4\mu})$ by

$$\begin{aligned} \alpha_{20} &= \beta_2 \cos\gamma, \\ \alpha_{22} &= \alpha_{2-2} = -\frac{1}{\sqrt{2}} \beta_2 \sin\gamma, \\ \alpha_{40} &= \frac{1}{6} \beta_4 (5\cos^2\gamma + 1), \\ \alpha_{42} &= \alpha_{4-2} = -\sqrt{\frac{5}{6}} \beta_4 \cos\gamma \sin\gamma, \\ \alpha_{44} &= \alpha_{4-4} = \sqrt{\frac{35}{72}} \beta_4 \sin^2\gamma, \end{aligned} \quad (32)$$

where the other $\alpha_{\lambda\mu}$ are zero.

As for the parameter set of the Woods-Saxon potential, i.e., the potential depth V_0, the nuclear radius R_0 and the diffuseness parameter a of the central potential, as well as those for the spin-orbit potential, we take the one provided recently by Wyss [32]; see Ref. [42] for actual values of the parameters. For proton, the Coulomb potential created by charge $(Z-1)e$ that has a uniform distribution inside the surface Σ is added to Eq. (29); more detailed description is explained elsewhere [43].

The deformation parameters in the Woods-Saxon potential can be determined by the standard Strutinsky (microscopic-macroscopic) method [44,45], where the pairing correlation is included within the BCS approximation. The monopole pairing interaction is used and its strength is determined according to the smoothed pairing gap method. As for the macroscopic part, the liquid-drop model of Ref. [46] is employed. The Ne isotopes in the island of inversion are sitting near the drip line. For such a case, the standard Strutinsky method has problems related to the continuum single-particle states. Recently the problems have been solved by using the so-called Kruppa prescription [47]. We use this improved method (the Kruppa-BCS method) to treat both the shell and pairing correlations.

As discussed in the following sections, we utilize different models for the analyses of reaction cross sections. In order to compare the deformation between different models, it is necessary to make a transformation between individual parameter sets, e.g., between $(\bar{\beta}, \bar{\gamma})$ in AMD and $(\beta_2, \gamma, \beta_4)$ in the Woods-Saxon model. This is made in the following way. The deformed surface in Eq. (31) determines the deformation parameters in the Woods-Saxon potential. We can define a uniform density with the sharp cut surface Σ determined by $R(\theta, \phi; \boldsymbol{\alpha})$ as

$$\rho_{\text{uni}}(\boldsymbol{r}) \equiv \rho_0 \theta(R(\theta, \phi; \boldsymbol{\alpha}) - r), \tag{33}$$

where ρ_0 is the average density and $\theta(x)$ is a step function, and we can calculate the expectation value of x^2 as

$$\langle x^2 \rangle_{\text{uni}} = \int x^2 \rho_{\text{uni}}(\boldsymbol{r}) d\boldsymbol{r}. \tag{34}$$

For given AMD deformation parameters $(\bar{\beta}, \bar{\gamma})$, the ratio of the AMD expectation values $\langle x^2 \rangle : \langle y^2 \rangle : \langle z^2 \rangle$ is fixed by Eqs. (19)−(21). Since the corresponding Woods-Saxon parameters $(\beta_2, \gamma, \beta_4)$ should be determined so as to give the same shape, one can impose the condition $\langle x^2 \rangle : \langle y^2 \rangle : \langle z^2 \rangle = \langle x^2 \rangle_{\text{uni}} : \langle y^2 \rangle_{\text{uni}} : \langle z^2 \rangle_{\text{uni}}$. This condition gives only two independent equations, so that the (β_2, γ) is determined under some fixed value of β_4. We set $\beta_4 = 0$ for simplicity in order to define (β_2, γ) values corresponding to the AMD calculation. The two pairs $(\bar{\beta}, \bar{\gamma})$ and (β_2, γ) take similar values to each other, as shown in Table V of Sec. III. We have also confirmed that the final reaction cross sections change very little (order of mb), even if β_4 is varied in the range $-0.1 < \beta_4 < 0.1$.

In the actual calculation, the Woods-Saxon potential is diagonalized with the anisotropic harmonic oscillator basis, where the three frequencies, ω_a ($a = x, y, z$), are taken to be proportional to $1/\sqrt{\langle a^2 \rangle_{\text{uni}}}$. This is close to the optimal choice. As for the basis size, we have used the oscillator shells $N_{\text{osc}} = n_x + n_y + n_z = 18$, and $N_{\text{osc}} = 18$ gives converged results in all calculated cases. To check convergence of calculated results, we have increased N_{osc} up to 20 for nuclei near the drip line, since the density distribution extends considerably there.

As in the Hartree-Fock (HF) or the Hartree-Fock-Bogoliubov (HFB) approach, the occurrence of deformation in the Woods-Saxon model is a symmetry-breaking phenomenon. The many-body wave function Φ is then considered to be that in the intrinsic (body-fixed) frame [48], and so is the nucleon

density calculated with Φ,

$$\rho^{(\text{in})}(\boldsymbol{r}) = \langle \Phi | \sum_i \delta(\boldsymbol{r}_i - \boldsymbol{r}) | \Phi \rangle = \sum_\alpha |\varphi_\alpha(\boldsymbol{r})|^2 v_\alpha^2, \tag{35}$$

where $\varphi_\alpha(\boldsymbol{r})$ is the Woods-Saxon single-particle wave function and v_α is the BCS occupation probability. In the BCS calculation, the free contributions should be subtracted when the Kruppa prescription is employed; see Refs. [47,49] for the details. Therefore the deformed density $\rho^{(\text{in})}(\boldsymbol{r}) = \rho^{(\text{in})}(r, \theta, \phi)$ cannot be directly used in the reaction theory such as the DFM that is formulated in the laboratory (space-fixed) frame.

One way to recover the spherical symmetry and transform the density in the intrinsic frame to that in the laboratory frame is to perform the AMP, as already explained in Eqs. (27) and (28) in the AMD framework. We have performed the projection calculation (without the c.m. correction, which is discussed in the next subsection) by using the method of Ref. [50] for the Woods-Saxon model with the BCS pairing correlation. It is found that the projected density $\rho_{II}^{(0)}(r)/\sqrt{4\pi}$, where $\rho_{II}^{(\lambda=0)}(r)$ is defined in the same way as in Eq. (28) and used in the DFM, is very similar to the following angle-averaged intrinsic density:

$$\rho_{\text{av}}^{(\text{in})}(r) = \frac{1}{4\pi} \int \rho^{(\text{in})}(r, \theta, \phi) \sin\theta d\theta d\phi. \tag{36}$$

In Fig. 1, they are compared for ^{30}Ne. As it is clear, for both neutron and proton, the projected and angle-averaged densities are almost identical particularly in the tail region, while slight differences are observed in the inner region for large I values. This is rather general trend, and therefore we use $\rho_{\text{av}}^{(\text{in})}(r)$ in place of $\rho_{II}^{(0)}(r)/\sqrt{4\pi}$ in the Woods-Saxon model for the ground state of Ne isotopes.

In the view of static behavior of deformed nuclei, using spherical part of deformed Woods-Saxon density, $\rho_{II}^{(0)}(r)/\sqrt{4\pi} \approx \rho_{\text{av}}(r)$, is well justified, but this procedure does not justify that dynamical aspect of deformation is also negligible. As already mentioned above, this point is argued in Sec. II E.
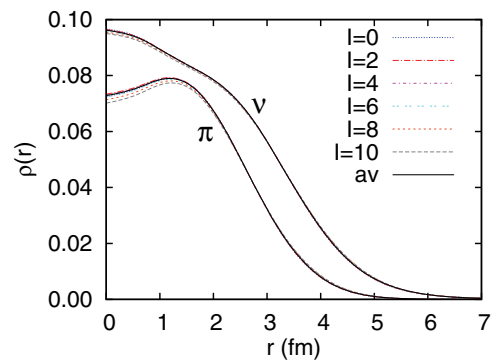

FIG. 1. (Color online) Comparison of the projected density, $\rho_{II}^{(0)}(r)/\sqrt{4\pi}$ with $I = 0, 2, \ldots, 10$, and the angle-averaged intrinsic density, $\rho_{\text{av}}^{(\text{in})}(r)$ in Eq. (36), for the Woods-Saxon model in ^{30}Ne. The deformation parameters are $\beta_2 = 0.4$ and $\gamma = \beta_4 = 0$, and the pairing gaps $\Delta_n = \Delta_p = 1$ MeV. The results are very similar also in the case with no pairing correlation.

D. Center-of-mass correction to nucleon density of the Woods-Saxon mean-field model

The projectile density is constructed with either AMD or the Woods-Saxon model for Ne isotopes. In contrast to AMD, the center-of-mass (c.m.) motion is not excluded in the many-body wave function Φ in the Woods-Saxon model. We thus extract the c.m. motion from Φ in the standard manner [51,52] and propose a simple extraction prescription consistent with the standard manner.

The wave function Φ is approximated by a product of the c.m. part $\Phi_{\mathrm{c.m.}}$ and the intrinsic part Φ_{int}:

$$\Phi = \Phi_{\mathrm{c.m.}} \Phi_{\mathrm{int}} \tag{37}$$

with

$$\Phi_{\mathrm{c.m.}} = \left(\frac{A}{\pi b^2}\right)^{3/4} \exp\left[-\frac{A}{2b^2}X^2\right] \tag{38}$$

for the c.m. coordinate X and the size parameter b. The mean squared radii of Φ and Φ_{int} are obtained by

$$\langle r^2 \rangle \equiv \langle \Phi | \sum_i r_i^2 | \Phi \rangle, \tag{39}$$

$$\langle r^2 \rangle_{\mathrm{int}} \equiv \langle \Phi_{\mathrm{int}} | \sum_i (r_i - X)^2 | \Phi_{\mathrm{int}} \rangle \tag{40}$$

for a single-particle coordinate r_i, and hence these are related to b as

$$\langle r^2 \rangle = \langle r^2 \rangle_{\mathrm{int}} + \frac{3}{2}\frac{b^2}{A}. \tag{41}$$

The c.m. correction to $\langle r^2 \rangle$ is small (order $1/A$), so it can be estimated with Φ instead of Φ_{int}:

$$\langle r^2 \rangle_{\mathrm{int}} \approx \langle \Phi | \sum_i (r_i - X)^2 | \Phi \rangle. \tag{42}$$

The correction is a combination of the one-body and two-body corrections. Inserting Eq. (42) into Eq. (41), one can determine the size parameter b and hence Φ_{int} from Φ.

The proton and neutron densities without and with the c.m. correction are respectively obtained by

$$\rho(r) = \langle \Phi | \sum_i \delta(r_i - r) P_i | \Phi \rangle, \tag{43}$$

$$\rho_{\mathrm{int}}(r) = \langle \Phi_{\mathrm{int}} | \sum_i \delta(r_i - X - r) P_i | \Phi_{\mathrm{int}} \rangle, \tag{44}$$

where P_i is a projector for proton or neutron. These densities satisfy

$$\rho(r) = \int dr' |\Phi_{\mathrm{c.m.}}(r - r')|^2 \rho_{\mathrm{int}}(r'). \tag{45}$$

The density ρ_{int} with the c.m. correction is thus obtained by unfolding ρ with $|\Phi_{\mathrm{c.m.}}|^2$.

Instead of the complicated unfolding procedure [51], one can take the following simple prescription. As shown in Eq. (41), the difference between $\langle r^2 \rangle$ and $\langle r^2 \rangle_{\mathrm{int}}$ is small, because it is of order $1/A$. This indicates that r dependence of $\rho_{\mathrm{int}}(r)$ is similar to that of $\rho(r)$. We can thus approximate $\rho_{\mathrm{int}}(r)$ by

$$\rho_{\mathrm{int}}(r) = \frac{1}{\alpha^3} \rho(r/\alpha) \tag{46}$$

with a scaling factor

$$\alpha = \sqrt{\frac{\langle r^2 \rangle_{\mathrm{int}}}{\langle r^2 \rangle}} = \sqrt{1 - \frac{3}{2A}\frac{b^2}{\langle r^2 \rangle}}, \tag{47}$$

where α has been determined to reproduce $\langle r^2 \rangle_{\mathrm{int}}$ of Eq. (42). The error of this simple prescription to the unfolding procedure is only 0.1% in σ_{R} for Ne isotopes. The simple prescription is used in this paper, whenever $\rho_{\mathrm{int}}(r)$ is evaluated in the mean-field model. The rms radii, $\sqrt{\langle r^2 \rangle}$ and $\sqrt{\langle r^2 \rangle_{\mathrm{int}}}$, without and with the c.m. correction are estimated with the spherical HF model, and the parameter b is evaluated with Eq. (41) from the rms radii. For each of Ne isotopes, we use a common b among the HF calculation and the spherical and deformed WS calculations, since the difference of $\sqrt{\langle r^2 \rangle}$ among these mean-field models are at most 6%, and the 6% error to the 1.5% c.m. correction is negligible.

E. Dynamical deformation and reorientation effects

When the projectile is deformed in the intrinsic frame, the deformation increases the radius of the projectile density in the space-fixed frame and eventually enhances the reaction cross section. This static deformation effect has already been included in the DFM through the AMP. Another effect to be considered is the dynamical deformation effect, that is, an effect of the rotational motion of the deformed projectile during the scattering. This effect on the reaction cross section is found to be small for intermediate-energy nucleus-nucleus scattering [30]. This was confirmed with the adiabatic approximation to the rotational motion of projectile and the eikonal approximation to the relative motion between a projectile and a target. In this subsection, the effect is investigated with no approximation.

In order to test the dynamical deformation effect, we consider the scattering of ^{30}Ne from ^{12}C at 240 MeV/nucleon and do a coupled-channel calculation between the 0^+ ground state and the first 2^+ state of ^{30}Ne. The projectile density is calculated by the deformed Woods-Saxon (DWS) model with the deformation evaluated by AMD. The coupling potentials in the coupled-channel calculation are obtained by the so-called single-folding model; namely, the nucleon-^{12}C potential is first evaluated by folding the Melbourne g-matrix interaction with the target density of ^{12}C and the coupling potentials are obtained by folding the nucleon-^{12}C potential with the projectile transition densities.

In the single-channel calculation with no dynamical deformation effect, the resultant reaction cross section is 1469 mb. This result overestimates the corresponding result of the DFM by about 10%, but it is accurate enough for the present test. In the coupled-channel calculation with the dynamical deformation effect from the first 2^+ state, the resulting reaction cross section is 1468 mb. Thus the dynamical rotation effect on the reaction cross section is estimated as less than 0.1% which is consistent with the evaluation shown in Ref. [30]. The integrated inelastic cross section to the first 2^+ state is 2.9 mb. This is 0.2 % of σ_{R}, indicating that $\sigma_{\mathrm{I}} \approx \sigma_{\mathrm{R}}$.

TABLE I. Reaction cross sections for ^{12}C + ^{12}C scattering at $E_{in} = 250.8$ MeV/nucleon and ^{12}C + ^{27}Al scattering at $E_{in} = 250.7$ MeV/nucleon. Results of three types of effective nucleon-nucleon interactions are compared with the corresponding data [53]. The cross sections are presented in units of mb.

Target	Exp. [53]	t_{LF} [58]	g_{MP} [20]	g_{MB} [20]
^{12}C	782.0 ± 10.0	917.7	793.1	795.9
^{27}Al	1159.0 ± 14.0	1337.5	1164.9	1185.2

The folding potential U is not spherical in general, when the spin of projectile is not zero. In this situation, one has to solve the coupled-channel equations (9). Effects of the nonspherical part of U on the elastic scattering, i.e., the reorientation effect, is also tested for the scattering of ^{31}Ne($3/2^-$) from ^{12}C at 240 MeV/nucleon, where the single-folding model is used. The resultant reaction cross section is 1512 mb, whereas the corresponding cross section is 1515 mb when the nonspherical part of U is switched off. The reorientation effect is 0.2% and hence negligible for intermediate-energy nucleus-nucleus scattering.

III. RESULTS

A. Reaction cross sections for stable nuclei

We first test the accuracy of the DFM with the Melbourne g-matrix nucleon-nucleon interaction for ^{12}C scattering at incident energies (E_{in}) around 240 MeV/nucleon from stable targets, ^{12}C, ^{20}Ne, ^{23}Na, and ^{27}Al. Experimental data on σ_R are available for a ^{12}C target at $E_{in} = 250.8$ MeV/nucleon and a ^{27}Al target at $E_{in} = 250.7$ MeV/nucleon [53]. For ^{20}Ne and ^{23}Na targets, σ_I at $E_{in} = 240$ MeV/nucleon were recently deduced from measured σ_I at around 1 GeV/nucleon [54,55] with the Glauber model [10].

For these stable nuclei, we take the phenomenological proton-density [56] deduced from the electron scattering by unfolding the finite-size effect of the proton charge in the standard manner [57], and the neutron density is assumed to have the same geometry as the corresponding proton one, since the proton rms radius deviates from the neutron one only by less than 1% in the Hartree-Fock (HF) calculation.

The DFM calculations are done with three types of effective nucleon-nucleon interactions: the Love-Franey t-matrix interaction (t_{LF}) [58], the Melbourne g-matrix interaction (g_{MP}) [20] evaluated from the Paris realistic nucleon-nucleon interaction [59] and the Melbourne interaction (g_{MB}) [20] constructed from the Bonn-B realistic nucleon-nucleon interaction [39].

Table I shows experimental and theoretical reaction cross sections for a ^{12}C target at $E_{in} = 250.8$ MeV/nucleon and a ^{27}Al target at $E_{in} = 250.7$ MeV/nucleon. The effective interaction t_{LF} has no nuclear medium effect. In this case, the theoretical reaction cross sections overestimate the mean values of data [53] by 17% for ^{12}C and by 15% for ^{27}Al. As for g_{MP} and g_{MB} with the medium effect, meanwhile, the overestimation is only a few percent for both ^{12}C and ^{27}Al. The medium effect is thus significant, and the amount of the effect is almost independent of the bare nucleon-nucleon interaction
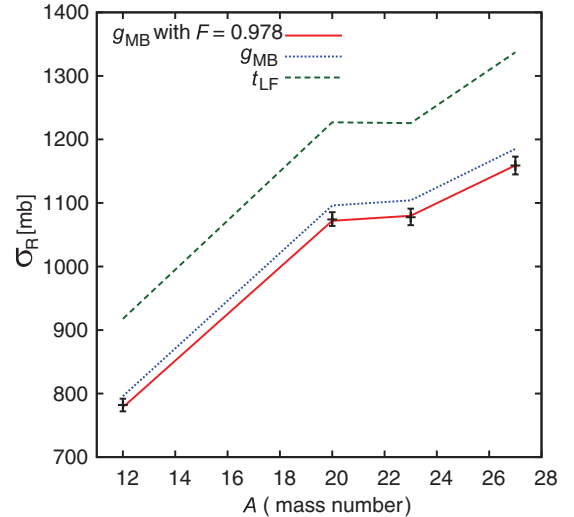

FIG. 2. (Color online) Reaction cross sections for scattering of ^{12}C on stable nuclei from $A = 12$ to 27. The data at 250.8 MeV/nucleon for ^{12}C and ^{27}Al are taken from Ref. [53]. The data at 240 MeV/nucleon for ^{20}Ne and ^{23}Na are deduced from measured σ_I at around 1 GeV/nucleon [54,55] with the Glauber model [10]. The solid (dotted) line stands for the results of DFM calculations with g_{MB} after (before) the normalization with $F = 0.978$, whereas the dashed line corresponds to results of t_{LF}.

taken. As for ^{27}Al, the reaction cross section calculated with g_{MB} agrees with the mean value of data, when the theoretical σ_R is multiplied by the factor $F = 0.978$.

In Fig. 2, the reaction cross sections are plotted for ^{12}C, ^{20}Ne, ^{23}Na, and ^{27}Al targets. The dotted and solid lines represent results of DFM calculations with g_{MB} before and after the normalization with $F = 0.978$, respectively. Before the normalization procedure, the DFM results (dotted line) slightly overestimate the mean values of data for $A = 20$–27. After the normalization procedure, the DFM results (solid line) agree with the mean values of data for all the targets. The normalization procedure is thus reliable. The dashed line corresponds to the results of DFM calculations with t_{LF} and no normalization. The medium effect reduces the theoretical reaction cross sections by about 15% for all the targets.

Figure 3 shows the results of DFM calculations for the angular distribution of ^{12}C + ^{12}C elastic scattering at (a) 135 MeV/nucleon and (b) 74.25 MeV. In panel (a) where the incident energy is close to 250 MeV/nucleon of our interest, the DFM calculation with g_{MB} (solid line) well reproduces the data [60], whereas that with t_{LF} (dashed line) does not. Also for the low incident energy in panel (b), the DFM calculation with g_{MB} (solid line) yields better agreement with the data [61] than that with t_{LF} (dashed line). For scattering angles larger than 50 degrees, the solid line does not reproduce the data perfectly. The deviation may come from effects of collective projectile and target excitations that are not included in the g-matrix. Thus the DFM with g_{MB} is quite reliable particularly for intermediate incident energies.

As for the scattering of Ne isotopes on ^{12}C at 240 MeV/nucleon, we have done DFM calculations with g_{MB} and the normalization factor F. The DFM calculation with
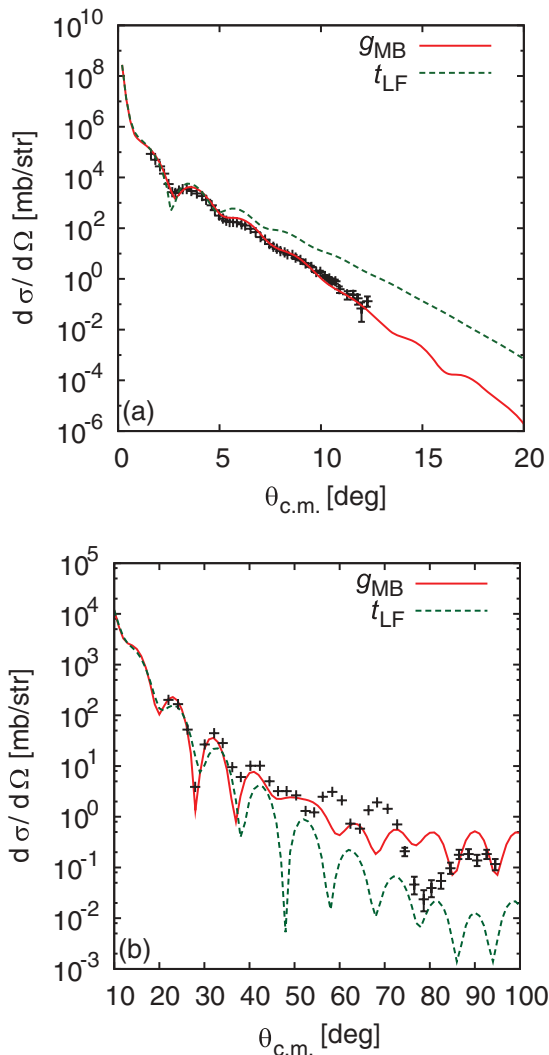
FIG. 3. (Color online) Angular distribution of $^{12}C + ^{12}C$ elastic cross section at (a) 135 MeV/nucleon and (b) 74.25 MeV. The solid (dashed) line stands for the results of DFM calculations with g_{MB} (t_{LF}). The data are taken from Ref. [60] in (a) and from Ref. [61] in (b).

g_{MB} has numerical ambiguity due to the parametrization of g_{MB}; the imaginary part of the folding potential has a small positive value in the tail region. If the positive imaginary part is cut, it increases the reaction cross section by 2% for a ^{12}C projectile and by 1% for Ne isotopes. This cut is used in this paper. If the cut is not taken, F becomes 1.0 and hence the resultant reaction cross sections for Ne isotopes are increased by 1% from the present results. This numerical ambiguity does not change any conclusion in this paper, since the ambiguity is tiny.

B. AMD analysis for Ne isotopes

Table II shows AMD results for the ground-state properties of Ne isotopes, i.e., the spin-parity (I^π), the one-neutron separation energy S_{-1n}, and the values of deformation parameters ($\bar{\beta}, \bar{\gamma}$). The AMD calculation yields the same I^π as

TABLE II. Ground-state properties of Ne isotopes predicted by AMD. For ^{28}Ne, the oblate state with $\bar{\beta} = 0.28$ is the main component of the ground state, but it is strongly mixed by the prolate state with $\bar{\beta} = 0.5$.

Nuclide	I^π(exp)	I^π(AMD)	S_{-1n} [MeV]	$\bar{\beta}$	$\bar{\gamma}$
^{20}Ne	0^+	0^+		0.46	$0°$
^{21}Ne	$3/2^+$	$3/2^+$	7.111	0.44	$0°$
^{22}Ne	0^+	0^+	9.779	0.39	$0°$
^{23}Ne	$5/2^+$	$5/2^+$	6.021	0.32	$0°$
^{24}Ne	0^+	0^+	8.231	0.25	$60°$
^{25}Ne	$1/2^+$	$1/2^+$	4.339	0.20	$31°$
^{26}Ne	0^+	0^+	5.153	0.22	$0.1°$
^{27}Ne	$(3/2^+)$	$3/2^+$	1.767	0.27	$13.6°$
^{28}Ne	0^+	0^+	3.123	0.28(0.50)	$60°(0°)$
^{29}Ne	$(3/2^+)$	$1/2^+$	1.321	0.43	$0°$
^{30}Ne	0^+	0^+	2.025	0.39	$0°$
^{31}Ne		$3/2^-$	0.248	0.41	$0°$
^{32}Ne	0^+	0^+	1.012	0.33	$0°$

the data displayed on the web site [62], although they are not established experimentally for $^{27,29,31}Ne$. Particularly for ^{31}Ne in the island of inversion, the ground state has $I^\pi = 3/2^-$ and small S_{-1n} consistent with the data 0.290 ± 1.640 MeV [63]. For ^{28}Ne corresponding to the boundary of the island of inversion, the main component of the ground state is the oblate state with $\bar{\beta} = 0.28$, but it is strongly mixed by the prolate state with $\bar{\beta} = 0.50$. The deformation parameter $\bar{\beta}$ decreases as A increases from 20 to 25 and increases as A increases from 25 to 32. The deformation becomes smallest at $A = 25$.

Figure 4 plots (a) the total binding energy and (b) S_{-1n} as a function of A; here the data are taken from Refs. [63,64]. In the HF and HFB calculations, the spherical shape is imposed with the filling approximation, and the nuclei with $A > 30$ are unbound. For the total binding energy shown in panel (a), the Gogny-HF calculation (dotted line) underestimates the data systematically. This situation is improved by the Gogny-HFB calculation (dashed line). The Gogny-AMD calculation (solid line) yields even better agreement with the data. For S_{-1n} shown in panel (b), the Gogny-HF calculation cannot reproduce the even-odd difference well, but this problem is resolved by the Gogny-HFB calculation. The pairing correlation is thus important for S_{-1n}. The Gogny-AMD calculation almost reproduces the measured even-odd difference for all Ne isotopes from $A = 21$ to 32. This may indicate that the pairing correlation is included, at least partly, in the Gogny-AMD calculation. The deformation parameter $\bar{\beta}$ is 0.33 for ^{32}Ne and 0.41 for ^{31}Ne. The reduction of $\bar{\beta}$ from 0.41 to 0.33 may come from the pairing effect.

Figure 5 represents σ_R for scattering of Ne isotopes on ^{12}C at 240 MeV/nucleon. The AMD calculation (solid line) succeeds in reproducing the data [10], while the spherical Gogny-HF calculation (dotted line) undershoots the data; note that the spherical Gogny-HFB calculation yields the same result as the spherical Gogny-HF calculation within the thickness of line. The enhancement from the dotted line to the solid line comes from the deformation of the ground state, since the deformation is the main difference between the two calculations. The
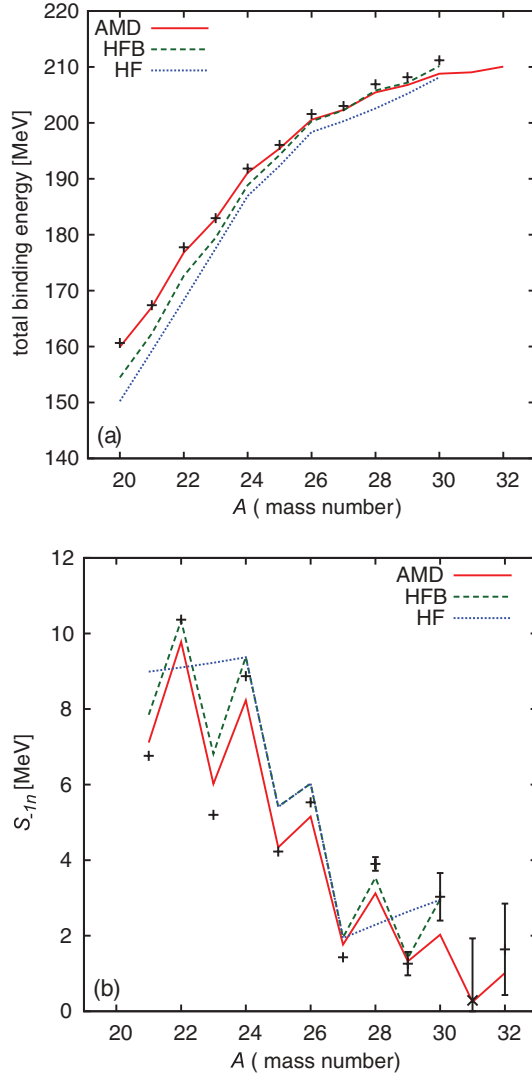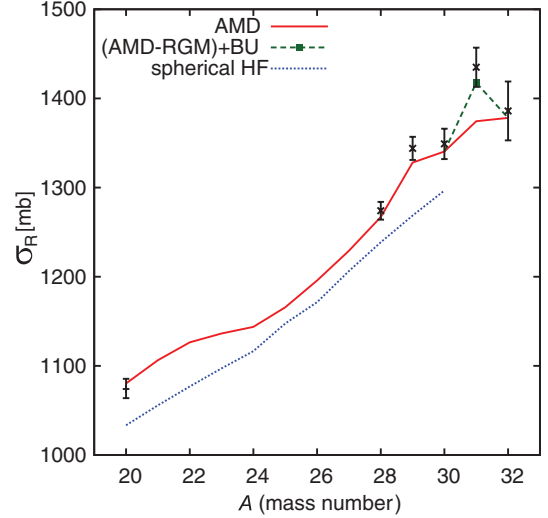
FIG. 5. (Color online) Reaction cross sections for the scattering of Ne isotopes on ^{12}C at 240 MeV/nucleon. The solid (dotted) line represents the results of the AMD (spherical Gogny-HF) calculations. The dashed line with a closed square is the AMD calculation with the tail and breakup corrections. The experimental data for $A = 28$–32 are taken from Ref. [10]. The data for ^{20}Ne are deduced from measured σ_I at around 1 GeV/nucleon [54] with the Glauber model [10].

where χ_n is the spin wave function of last neutron and $R_{ilj}(r)Y_{lm}(\hat{r})$ is the relative wave function between the last neutron and the core (^{30}Ne). As the excitation of ^{30}Ne, we consider the excited states $\Phi(^{30}\text{Ne}; I_i^\pi)$ with positive- and negative-parity below 10 MeV in excitation energy. This AMD-RGM calculation is quite time consuming, but it has been performed for ^{31}Ne. The tail correction to σ_R is 35 mb.

For weakly bound systems such as ^{31}Ne, furthermore, the projectile breakup is not perfectly negligible. This effect is simply estimated by assuming the potential model for the $^{30}\text{Ne} + n$ system and solving the three-body dynamics of the $^{30}\text{Ne} + n + {}^{12}$C system with the method of continuum discretized coupled channels (CDCC) [65,66]. CDCC is an accurate method for treating exclusive reactions such as elastic scattering and elastic-breakup reactions. The theoretical foundation of CDCC is shown in Refs. [67–69]. CDCC has succeeded in reproducing data on the scattering of stable and unstable projectiles [65,66,70–83]. In the present calculation the interactions between ^{30}Ne and ^{12}C and between n and ^{12}C are constructed by the DFM calculation with the Melbourne g-matrix, and the potential between ^{30}Ne and n is made with the well-depth method; see Refs. [23,84] for the potential parameters. The correction is 10 mb corresponding to 0.7% of σ_R. In Fig. 5, the dashed line stands for the AMD result with the tail and breakup corrections for ^{31}Ne. The result is consistent with the data for ^{31}Ne.

The reaction cross section σ_R is sensitive to the rms radii, $\sqrt{\langle r^2\rangle_P}$ and $\sqrt{\langle r^2\rangle_T}$, of projectile and target, respectively. Actually, the DFM calculations for $^{20-32}$Ne projectiles show that

$$\sigma_R = C\pi[\sqrt{\langle r^2\rangle_P} + \sqrt{\langle r^2\rangle_T}]^2, \quad (49)$$

FIG. 4. (Color online) Results of the AMD, the spherical Gogny-HF and the spherical Gogny-HFB calculation for (a) the total binding energy and (b) the one-neutron separation energy of Ne isotopes. The dotted, dashed and solid lines represent results of the Gogny-HF, Gogny-HFB, and AMD calculations. In the spherical HF calculations, the nuclei with $A > 30$ are unbound. The experimental data are taken from Refs. [63,64].

AMD results are consistent with all the data except ^{31}Ne. The underestimation of the AMD result for ^{31}Ne comes from the inaccuracy of the AMD density in its tail region.

The tail problem is solved by the following resonating group method (RGM) [31]. In principle the ground state $\Phi(^{31}\text{Ne}; 3/2_1^-)$ of ^{31}Ne can be expanded in terms of the ground and excited states $\Phi(^{30}\text{Ne}; I_i^\pi)$ of ^{30}Ne. This means that the ground state of ^{31}Ne is described by the $^{30}\text{Ne} + n$ cluster model with core (^{30}Ne) excitations. The cluster-model calculation can be done with the RGM in which the ground and excited states of ^{30}Ne are constructed by AMD:

$$\Phi(^{31}\text{Ne}; 3/2_1^-)$$
$$= \sum_{iljI\pi} \mathcal{A}\left\{ R_{ilj}(r)\left[[Y_l(\hat{r})\chi_n]_j \Phi(^{30}\text{Ne}; I_i^\pi)\right]_{3/2}^{(-)}\right\}, \quad (48)$$
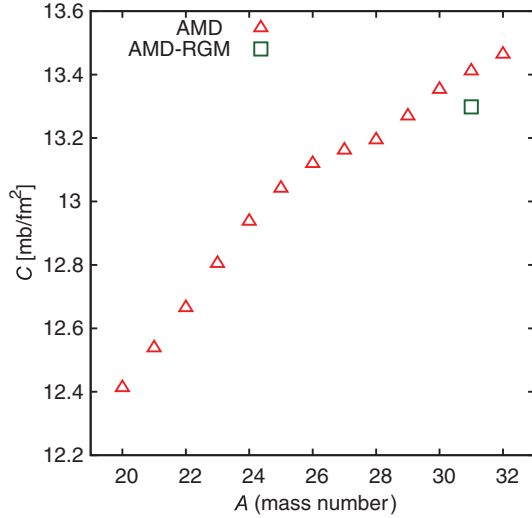
FIG. 6. (Color online) A dependence of the coefficient C. Opened triangles show the results of the AMD calculations, whereas an opened square corresponds to the result of the AMD-RGM calculation for ^{31}Ne.
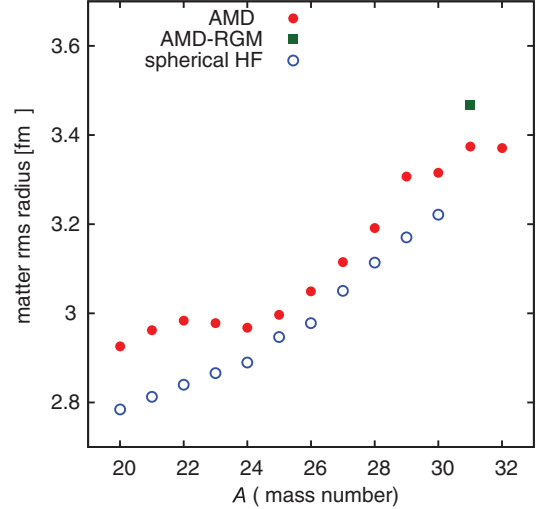

FIG. 7. (Color online) Matter rms radii of Ne isotopes calculated with the AMD, the AMD-RGM, and the spherical HF model. The closed circle represents the results of the AMD, and the closed square denotes the result of the AMD-RGM model for ^{31}Ne. The opened circles are the results of the spherical HF calculation.

where C is a slowly varying function of A around $C = 12.4 \sim 13.5$ mb/fm^2, as shown in Fig. 6. If the volume conservation is imposed with the general shape in Eq. (31), the matter squared radius $\langle \mathbf{r}^2 \rangle_{\mathrm{P}}$ of projectile is described by

$$\langle \mathbf{r}^2 \rangle_{\mathrm{P}} = \langle \mathbf{r}^2 \rangle_0 \left[1 + \frac{5}{4\pi} \sum_{\lambda\mu} |\alpha_{\lambda\mu}|^2 \right] \tag{50}$$

$$= \langle \mathbf{r}^2 \rangle_0 \left[1 + \frac{5}{4\pi} \left(\beta_2^2 + \beta_4^2 + \cdots \right) \right] \tag{51}$$

up to the second order in the deformation parameters $\{\alpha_{\lambda\mu}\}$, where $\langle \mathbf{r}^2 \rangle_0$ is the matter squared radius in the spherical limit. Here the projectile density has been assumed to have a deformed well shape. The triaxial parameter γ does not appear in Eq. (51). This means that the triaxial deformation little affects the rms radius and hence σ_{R}. This can be tested by varying γ in the Woods-Saxon model. The reaction cross section changes only by 0.2% for ^{27}Ne, when γ is varied from $0°$ to $60°$ with fixing $\beta_2 = 0.273$ and $\beta_4 = 0$.

Figure 7 shows the rms radii of spherical-HF, AMD, AMD-RGM calculations. Differences among the three calculations are similar to those for σ_{R} shown in Fig. 5. The difference between AMD and AMD-RGM calculations for ^{31}Ne is appreciable, indicating that the tail correction is significant for this very weakly bound system.

Next we compare the neutron rms radius $\sqrt{\langle \mathbf{r}_n^2 \rangle}$ with the proton one $\sqrt{\langle \mathbf{r}_p^2 \rangle}$ in order to see the isovector components of the Ne-isotope densities. Figure 8 shows the A dependence of $\sqrt{\langle \mathbf{r}_n^2 \rangle}$ and $\sqrt{\langle \mathbf{r}_p^2 \rangle}$ for Ne isotopes. In panel (a), the neutron and proton rms radii increase with A, when $A \geqslant 24$. For $A = 20–24$, the proton rms radii have a bump. This indicates that for $A = 20–22$ the proton-neutron correlation is strong and hence the α-clustering grows. Panel (b) shows the difference $\sqrt{\langle \mathbf{r}_n^2 \rangle} - \sqrt{\langle \mathbf{r}_p^2 \rangle}$ as a function of A. The difference also goes up as A increases. There is a sizable jump between $A = 28$ and 29, since the deformation $\bar{\beta}$ is around 0.25 for $A = 24–28$

but around 0.4 for $A = 29–32$. As a result of this gap, the radius difference is around 0.35 fm for $A = 29$, 30, and 32. This indicates that Ne isotopes have a skin structure there. For $A = 31$, the radius difference calculated with the AMD-RGM method is about 0.5 fm that is significantly larger than 0.35 fm. This implies that ^{31}Ne is a halo nucleus. These interpretations are more obvious through the neutron and proton density profiles shown in Fig. 9. Panels (a)–(e) show the density profiles for $^{28–32}$Ne, respectively. Obviously ^{29,30,32}Ne have the neutron-skin structure. In panel (f), the density profile for ^{31}Ne is plotted on a logarithmic scale. The neutron density (dashed line) calculated with the AMD-RGM method has a long-range tail, indicating that ^{31}Ne has a halo structure.

In neutron-rich nuclear matter, some versions of the Gogny interactions are compared [85,86]. We then briefly consider the Gogny-D1N interaction [87] to see how AMD results depend on the interactions. Table III shows $\bar{\beta}$, $\bar{\gamma}$ and S_{-1n} calculated with the Gogny-D1N interaction for $^{30–32}$Ne. The values of $\bar{\beta}$ and $\bar{\gamma}$ for the Gogny-D1N interaction are almost the same as the corresponding values in Table II for the Gogny-D1S interaction. As for S_{-1n}, the value for the Gogny-D1N interaction is a bit larger than that for the Gogny-D1S interaction, although both the values are consistent with the data. Only a difference between the two interactions appears at the spin-parity of ^{31}Ne; it is $3/2^-$ for the Gogny-D1S interaction and $3/2^+$ for the Gogny-D1N interaction. Thus any significant difference does not appear for ^{30,32}Ne. For the structure of ^{31}Ne, meanwhile, detailed analyses are highly expected, since it is quite interesting whether ^{31}Ne has a halo structure when the spin-parity is $3/2^+$. We will discuss this point in a forthcoming paper.

C. Woods-Saxon mean-field model

In this subsection, results of the Woods-Saxon mean-field model are investigated. First, the spherical case is studied to
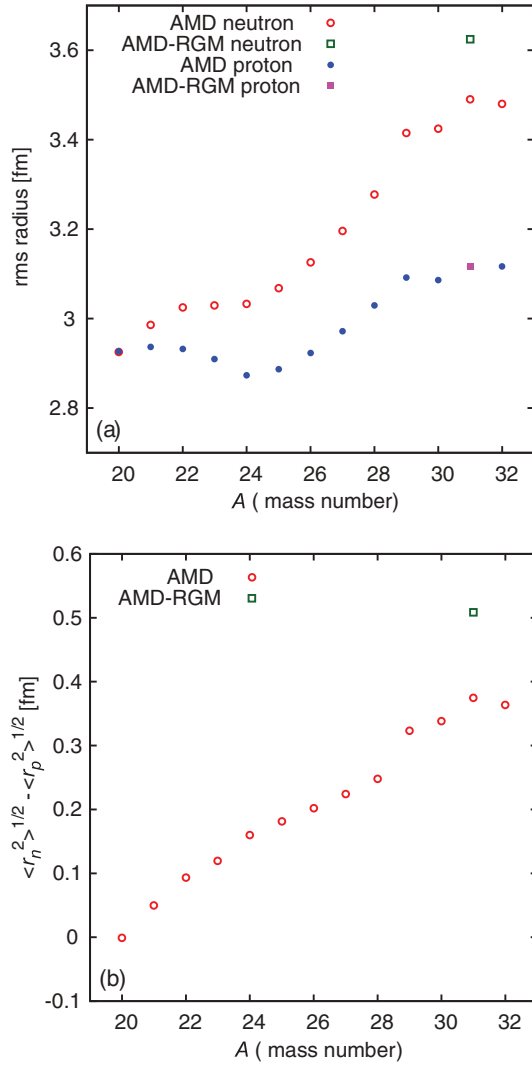
FIG. 8. (Color online) Neutron and proton rms radii of Ne isotopes calculated with the AMD and the AMD-RGM model. In (a), the closed (opened) circle represents the proton (neutron) rms radius calculated with the AMD and the closed (opened) square denotes the result of the AMD-RGM calculation for proton (neutron) of ^{31}Ne; note that the AMD-RGM result agrees with the AMD result for proton rms radius. (b) shows the difference between neutron and proton rms radii. The opened circle (square) stands for the AMD (AMD-RGM) result.

FIG. 9. (Color online) Neutron and proton density profiles for (a) ^{28}Ne, (b) ^{29}Ne, (c) ^{30}Ne, (d) ^{31}Ne, and (e) ^{32}Ne on a linear scale and (f) ^{31}Ne on a logarithmic scale. In (a)–(f), the solid (dotted) line presents the neutron (proton) density profile calculated with the AMD method, whereas the dashed line in (f) is the neutron density profile calculated with the AMD-RGM method.

justify the present parameter set of the Woods-Saxon model. Figure 10 shows the reaction cross sections for Ne isotopes calculated with the spherical Woods-Saxon (SWS) model (neglecting the pairing correlation) and the spherical Gogny-HF method. The SWS model (dotted line) well simulates the results of the spherical Gogny-HF calculation (solid line). This means that the SWS model yields almost the same matter radius as that of the spherical Gogny-HF calculation. The SWS model with the present parameter set proposed by Wyss [32] is thus a handy way of simulating the spherical Gogny-HF calculation.

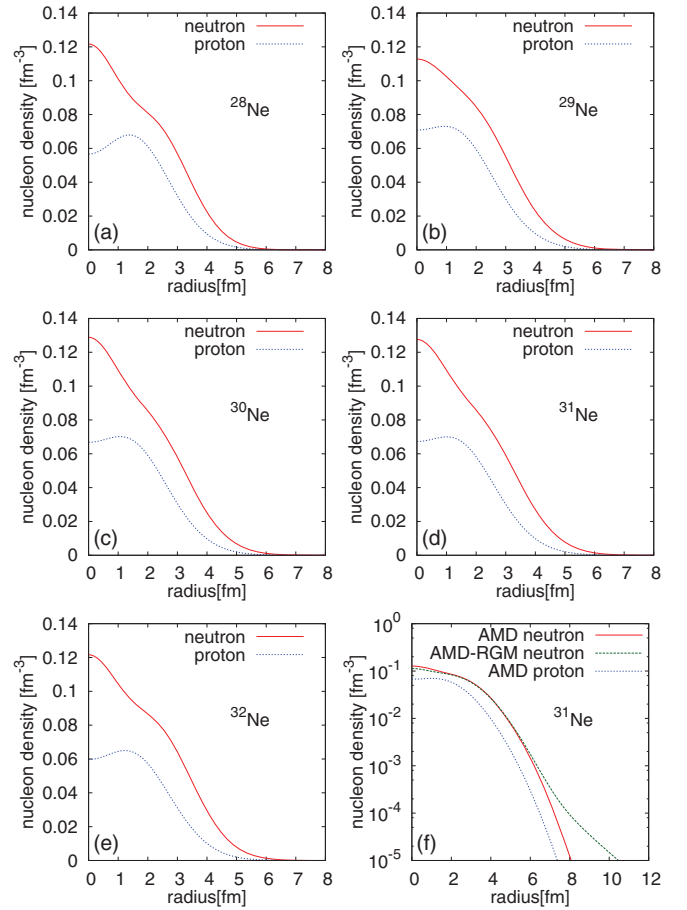Figure 11 shows the neutron Nilsson diagram for ^{30}Ne calculated with the deformed Woods-Saxon (DWS) model. It

is emphasized that the relatively large shell gap with $N = 20$ is observed at the spherical shape ($\beta_2 = 0$). Comparing this figure with the Nilsson diagram (Fig. 2 of Ref. [28]) calculated with the AMD model, one can see that the Nilsson diagram of the DWS model is close to that of the AMD model. In both the models, the [2,0,0,1/2] and the [3,3,0,1/2] orbit in terms of the Nilsson asymptotic quantum numbers [N, n_3, Λ, Ω] cross each other at $\beta_2 \approx 0.4$, although the single-particle energy at the crossing point is -3 MeV in the AMD model and -4 MeV in the DWS model. It is well known that the occupation of this down-sloping orbit [3,3,0,1/2] derives the system to deform near $N \approx 20$.

TABLE III. Ground-state properties of $^{30-32}$Ne predicted by AMD with the Gogny-D1N interaction.

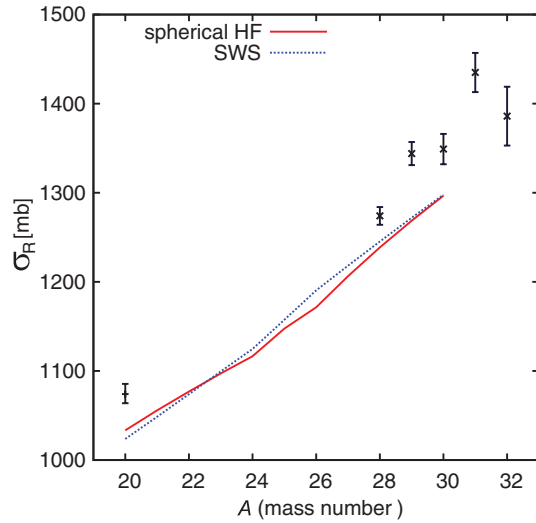| Nuclide	I^π(exp)	I^π(AMD)	S_{-1n} [MeV]	$\bar{\beta}$	$\bar{\gamma}$
^{30}Ne	0^+	0^+		0.39	$0°$
^{31}Ne		$3/2^+$	1.1	0.40	$0°$
^{32}Ne	0^+	0^+	1.6	0.28	$0°$

FIG. 10. (Color online) Reaction cross sections for Ne isotopes calculated with the SWS model and the Gogny-HF method. The spherical shape is imposed for both the calculations. The dotted line represents the results of the SWS model, while the solid line corresponds to the spherical Gogny-HF results. The nucleus with $A > 30$ are unbound. The experimental data are taken from Ref. [10].

Next, the equilibrium deformations of Ne isotopes are calculated in the DWS model by the microscopic-macroscopic (Strutinsky) method. The pairing correlation is included within the Kruppa-BCS approximation [47]. Here we consider two types of pairing strengths, $\widetilde{\Delta} = 12/\sqrt{A}$ and $4/\sqrt{A}$ MeV, determined from the smoothed pairing gap. The strength $\widetilde{\Delta} = 12/\sqrt{A}$ MeV is a typical value yielding the average even-odd mass differences. It has been pointed out [88], however, that in the light mass nuclei the even-odd mass
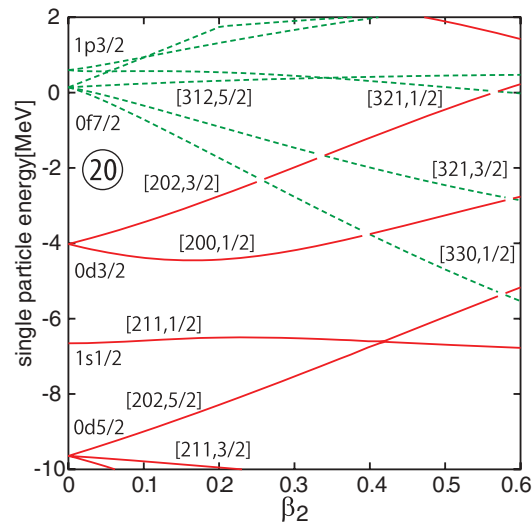

FIG. 11. (Color online) The neutron Nilsson diagram for ^{30}Ne in the deformed WS model, where the other parameters are fixed to $\beta_4 = \gamma = 0$. The solid (dashed) lines correspond to the positive (negative) parity orbits. The Nilsson asymptotic quantum numbers $[N, n_3, \Lambda, \Omega]$ are attached. The number 20 stands for a neutron magic number in the spherical limit.

TABLE IV. Deformation parameters (β_2, β_4) extracted from the results of deformed Gogny-D1S HFB calculations of Refs. [90,91]. The nucleus ^{31}Ne is unbound and no data are available.

Nuclide	β_2	β_4
^{20}Ne	0.325	0.108
^{21}Ne	0.370	0.085
^{22}Ne	0.355	0.016
^{23}Ne	0.234	0.011
^{24}Ne	0.179	0.011
^{25}Ne	-0.047	0.001
^{26}Ne	-0.002	0.000
^{27}Ne	-0.073	-0.005
^{28}Ne	-0.006	0.000
^{29}Ne	-0.060	-0.003
^{30}Ne	-0.002	0.000
^{31}Ne	—	—
^{32}Ne	0.246	0.096

differences contain considerable amount of the shell effect of deformed mean-field and thereby the actual pairing correlation becomes weaker. This situation is simulated by the smaller value $\widetilde{\Delta} = 4/\sqrt{A}$ MeV. All nuclei are calculated to be axially symmetric in their ground states, and the obtained deformations are smaller than those obtained by the AMD calculation. If the standard pairing is used, all even-even isotopes turn out to be spherical. Even with the weaker pairing, ^{25,26,28,30}Ne are calculated to be spherical, because of the relatively large $N = 20$ shell gap; see Fig. 11 for the shell gap. This result is in contrast to the prediction based on the tensor force in Ref. [89]. Although the binding energies and the one-neutron separation energies are rather well reproduced in the microscopic-macroscopic method, the calculated reaction cross sections are smaller in the island of inversion (not shown); this is due to the fact that the obtained equilibrium deformations are too small.

In order to confirm that the simple mean-field model does not give large deformations in the island of inversion, we show the deformations obtained by the systematic Gogny-D1S HFB calculations [90], the results of which are available on the web site [91]. The (β_2, β_4) deformation parameters are listed in Table IV, which are extracted in such a way that $\langle r^2 Y_{20} \rangle_{\mathrm{uni}}/\langle r^2 \rangle_{\mathrm{uni}}$ and $\langle r^4 Y_{40} \rangle_{\mathrm{uni}}/\langle r^2 \rangle_{\mathrm{uni}}^2$ calculated with the uniform density in Eq. (33) reproduce the corresponding values of Gogny-D1S HFB calculations tabulated in [91]. It is clear that the obtained deformations are smaller than those of the AMD calculation in Table II, and similar to those of the Strutinsky calculations (not shown). The reason why the AMD calculation gives larger deformations particularly in the island of inversion is that the optimum deformation is searched after the AMP; note that the same Gogny-D1S force is used in the HFB calculation of Refs. [90,91]. It is known that the potential energy surface as a function of quadrupole deformation is rather shallow for nuclei in the island of inversion. In such a case, the energy gain of the AMP at large deformation can easily change the equilibrium deformation, see, e.g., Ref. [27] for Ne isotopes. The AMP is thus important for the island of inversion to obtain large deformations.

TABLE V. Deformation parameter β_2 and γ deduced from the AMD intrinsic density. Those with higher multipoles $\lambda > 2$ are not included. The Nilsson asymptotic quantum numbers of last neutron are included as the last column for axially symmetric cases.

Nuclide	$\bar{\beta}$	$\bar{\gamma}$	β_2	γ	$[N, n_3, \Lambda, \Omega]$ for last-n
^{20}Ne	0.46	0°	0.479	0°	[2,2,0,1/2]
^{21}Ne	0.44	0°	0.456	0°	[2,1,1,3/2]
^{22}Ne	0.39	0°	0.400	0°	[2,1,1,3/2]
^{23}Ne	0.32	0°	0.325	0°	[2,0,2,5/2]
^{24}Ne	0.25	60°	0.258	60°	[2,0,0,1/2]
^{25}Ne	0.20	31°	0.202	31.5°	
^{26}Ne	0.22	0.1°	0.221	0°	[2,1,1,1/2]
^{27}Ne	0.27	13.6°	0.273	14.1°	
^{28}Ne	0.50	0°	0.526	0°	[3,3,0,1/2]
	0.28	60°	0.291	60°	[2,1,1,3/2]
^{29}Ne	0.43	0°	0.445	0°	[2,0,0,1/2]
^{30}Ne	0.39	0°	0.400	0°	[2,0,0,1/2]
^{31}Ne	0.41	0°	0.422	0°	[3,2,1,3/2]
^{32}Ne	0.33	0°	0.335	0°	[2,0,2,3/2]

D. Woods-Saxon model with AMD deformation

In the previous subsection, it was shown that both the microscopic-macroscopic calculation in the DWS model and the deformed Gogny-D1S HFB calculation (without the AMP) do not yield large deformations expected in the island of inversion. In this subsection we then consider the DWS model with the AMD deformation and compare the results with the AMD results. The pairing correlation is discussed at the end of this subsection.

Table V lists up the deformation parameters β_2 and γ deduced from the corresponding AMD values $\bar{\beta}$ and $\bar{\gamma}$ and used in the following DWS calculations. In Fig. 12, the matter rms radius calculated with the DWS model is compared with those of AMD and AMD-RGM calculations. The DWS model
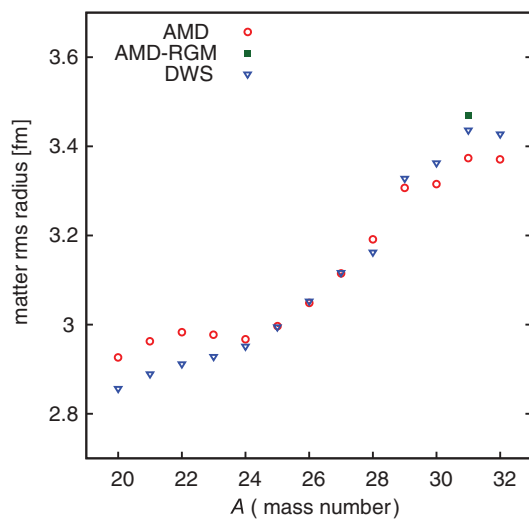

FIG. 12. (Color online) Matter rms radii of Ne isotopes calculated with the DWS, AMD, and AMD-RGM models. The opened circles represent the results of the AMD model, and the closed square denotes the result of the AMD-RGM model for ^{31}Ne. The opened inverted triangles are the results of the deformed Woods-Saxon calculation.
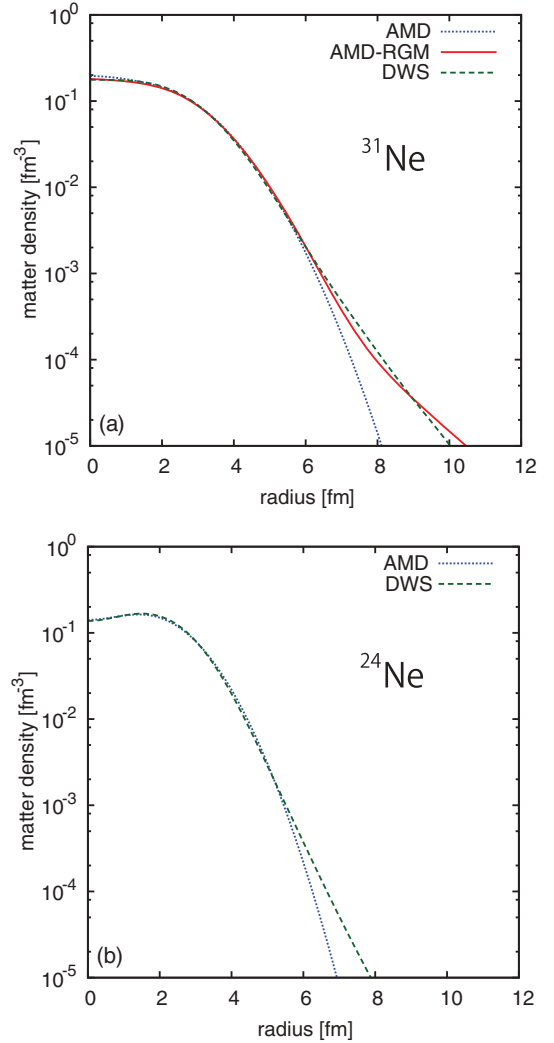

FIG. 13. (Color online) Density distributions of (a) ^{31}Ne and (b) ^{24}Ne. The dotted line represents the result of the AMD model, whereas the dashed line corresponds to the result of the DWS model. The solid line is the result of the AMD-RGM model.

well reproduces the matter rms radii of AMD calculations for $^{24-29}$Ne of which S_{-1n} is large. For $^{30-32}$Ne of which S_{-1n} is small, the matter rms radii of AMD calculations are slightly smaller than those of the DWS model. The deviation may come from the fact that the AMD densities are inaccurate in the tail region, since the DWS model almost reproduces the matter rms radius of the AMD-RGM calculation for ^{31}Ne. For $^{20-23}$Ne, the matter rms radii of AMD calculations are larger than those of the DWS model. This implies that the α-clustering is well developed in AMD calculations so that deformations not included in the present Woods-Saxon model, e.g., the octupole deformation ($\alpha_{3\mu}$), becomes important.

The nucleon density distributions are plotted in Fig. 13 for ^{24}Ne and ^{31}Ne. The AMD densities (dotted curves) decrease with increasing r more rapidly than the densities of the DWS model (dashed curves). The deviation between the two densities at large r is rather small for ^{24}Ne where S_{-1n} is large. The deviation is, however, enlarged for ^{31}Ne of which S_{-1n} is small. The AMD density is thus inaccurate at large r
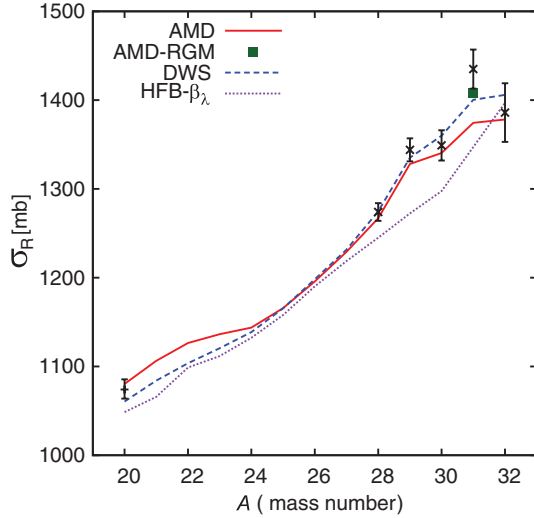
FIG. 14. (Color online) Reaction cross sections for Ne isotopes calculated with the DWS, AMD, and AMD-RGM models. The dashed line represents the results of the DWS model, while the solid line corresponds to the AMD results. The result of the DWS with the deformation determined by the deformed Gogny-D1S HFB calculation (Table IV) is also included as the dotted line. The closed square represents the result of the AMD-RGM calculation without breakup contribution. The experimental data are taken from Ref. [10].

particularly for ^{31}Ne. The tail correction to the AMD density can be made by the AMD-RGM calculation. The density (solid curve) has actually a long-range tail and consequently becomes close to that of the DWS model. As an important result, the density of the DWS model almost agrees with that of the AMD-RGM calculation for ^{31}Ne. This result indicates that the DWS model with the AMD deformation is a handy way of making a tail correction to the AMD density.

Figure 14 shows the reaction cross sections for Ne isotopes. The DWS model with AMD deformation gives σ_R consistent with the experimental data [10]. Comparing Fig. 14 with Fig. 12, one can see that A dependence of σ_R is similar to that of the matter rms radius for each of DWS, AMD, and AMD-RGM calculations. The DWS model with HFB deformation [90,91] yields much smaller σ_R in the island of inversion than the DWS model with AMD deformation. The AMP is thus important to evaluate σ_R properly. As another important result, the DWS model with AMD deformation gives almost the same σ_R as the AMD model for $^{24-29}$Ne and as the AMD-RGM model for ^{31}Ne. This indicates that the DWS model with AMD deformation is a simple of making the tail correction to the AMD density. The difference between the DWS model with AMD deformation and the AMD model for ^{30,32}Ne shows the amount of the tail correction.

Figure 15 shows effects of the pairing correlation on the total binding energy, S_{-1n} and σ_R. The dashed and dotted lines represent results of the standard pairing strength $\widetilde{\Delta} = 12/\sqrt{A}$ MeV and the weaker one $\widetilde{\Delta} = 4/\sqrt{A}$ MeV, respectively. The DWS model with AMD deformation well reproduces the measured total binding energy [63,64], even if the pairing is switched off. The pairing effects are more significant for S_{-1n} than for the total binding energy, as
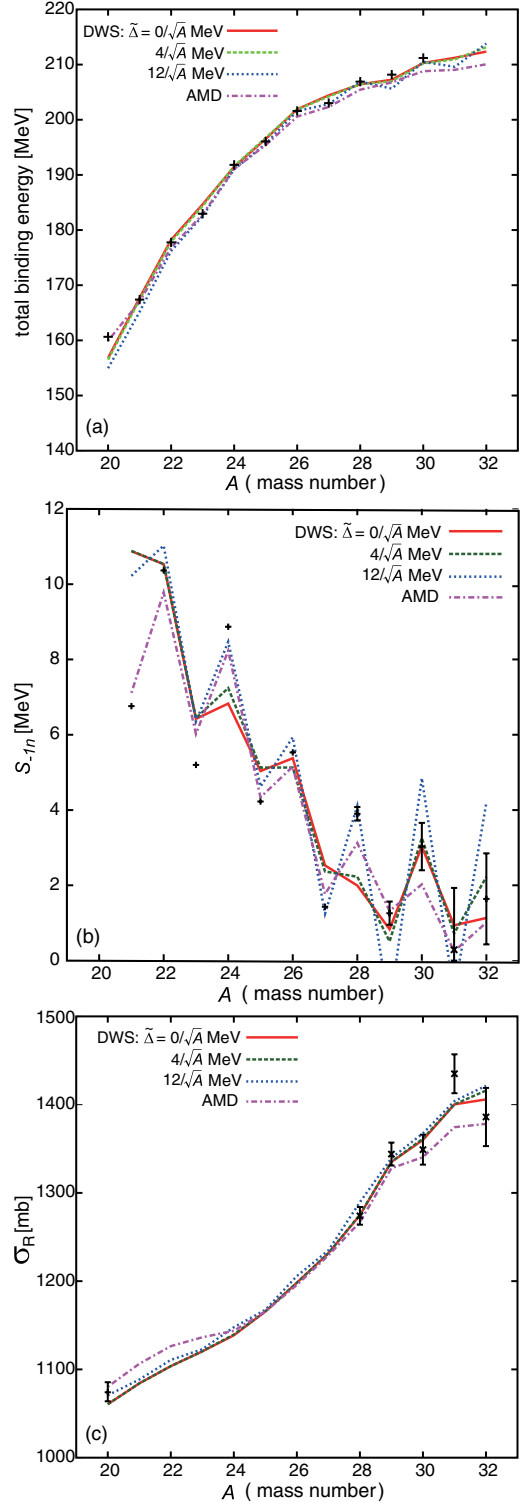

FIG. 15. (Color online) Pairing effects on (a) the total binding energy, (b) the one-neutron separation energy S_{-1n}, and (c) the reaction cross sections σ_R for Ne isotopes. The solid line is the result of the DWS model without pairing correction and the dashed (dotted) lines stand for the result of the DWS model including the pairing correlation with $\tilde{\Delta} = 4/\sqrt{A}$ ($12/\sqrt{A}$) MeV. In (a) and (b) the dot-dashed line represents the results of AMD, whereas in (c) the line means σ_R calculated with the AMD density. The experimental data are taken from Refs. [63,64] in (a) and (b), and from Ref. [10] in (c).

expected. In the DWS model, the even-odd difference in S_{-1n} is too much enhanced for $^{29-32}$Ne, if the standard pairing strength is used, while a better fitting is obtained with the weaker pairing strength. The S_{-1n} calculated with AMD (dot-dashed line) is close to the result of the standard paring strength for $^{21-28}$Ne and to the result of the weaker pairing strength for $^{29-32}$Ne, so that AMD almost reproduces the measured S_{-1n}. This indicates that AMD includes the paring correlation at least partly. The reaction cross sections are slightly enhanced by the pairing correlation, but the effect is small even with the standard pairing strength.

For weakly bound systems, it is speculated that the pairing correlation leads to an extra binding of halo orbit and makes the nuclear radius shrink; it is called the "pairing anti-halo" effect [92,93]. Our Kruppa-BCS method can produce the anti-halo like effect [49], but a reduction due to the pairing effect is not observed in the present calculations. Possible reasons are the large deformations, which tend to prevent the anti-halo effect, and that the binding of the last neutron orbit is not weak enough. As a future work, the deformed AMP-HFB calculation is highly expected to answer whether the "pairing anti-halo" effect really occurs and reflects the reaction cross section.

In the DWS model that corresponds to the AMD model with the tail correction, σ_R for ^{32}Ne is slightly larger than that for ^{31}Ne as shown in Fig. 14, but the rms radius for ^{32}Ne is smaller than that for ^{31}Ne as presented in Fig. 12. The reduction of the rms radius comes from that of β_2. It is interesting to consider what causes the reduction of β_2. This is another interesting future subject related to the "pairing anti-halo" effect mentioned above.

IV. SUMMARY

We have determined deformations of $^{20-32}$Ne by using the fully microscopic AMD model with the Gogny-D1S interaction. The quadrupole deformation parameter determined is around 0.4 in the island of inversion. The AMD model has no adjustable parameter, but the tail of the density is inaccurate particularly for weakly bound systems such as ^{31}Ne. We have made a tail correction to the AMD density for ^{31}Ne by using the AMD-RGM method. The resultant matter density has a halo structure and hence ^{31}Ne is a halo nucleus with large deformation.

We have analyzed the measured interaction cross sections [10] for $^{20,28-32}$Ne with the DFM in order to verify the theoretical prediction mentioned above. The microscopic reaction model with the Melbourne g-matrix yields good agreement with the measured interaction cross sections, if the projectile

densities are constructed by the AMD model for $^{20,28-30,32}$Ne and the AMD-RGM model for ^{31}Ne. We can thus conclude that the theoretical prediction mentioned above is reliable. In this analysis, the interaction cross section is assumed to be identical with the reaction cross section. The difference between the two cross sections comes from projectile excitations to its discrete states. It has been confirmed by coupled-channel calculations that the difference is small.

Since the AMD-RGM calculation is quite time consuming, as an alternative to the calculation we have considered the Woods-Saxon mean-field model with the deformation obtained by the AMD calculation. This deformed Woods-Saxon (DWS) model provides the matter density with the proper asymptotic form, but the parameter set of the Woods-Saxon potential should be carefully chosen. The parameter set recently proposed by Wyss [32] is quite successful, since the DWS model yields almost the same matter density as the AMD-RGM method for ^{31}Ne. This means that the DWS model is a handy way of simulating the AMD-RGM calculation.

The DWS model is quite useful to understand dynamics of many-body systems. When the microscopic-macroscopic (Strutinsky) calculations are done in the Woods-Saxon model, the obtained deformations are too small for $^{28-32}$Ne. This result is consistent with the deformed HFB calculations with no angular momentum projection in this region. This shows that the angular momentum projection is essential to obtain the large deformations in $^{28-32}$Ne. It is also easy to add the BCS-type pairing correlation to the model. The result shows that the pairing effect is small in $^{28-32}$Ne.

Throughout these results, we propose, as a useful and convenient microscopic approach, the combination of the DFM with the Melbourne g-matrix and the DWS model with the AMD deformation. The microscopic approach provides the density with the proper asymptotic form and has no adjustable parameter. The microscopic approach well reproduces the measured interaction cross sections for $^{20,28-32}$Ne. It is thus highly expected that the microscopic approach is applied to other scattering systems.

[1] E. K. Warburton, J. A. Becker, and B. A. Brown, Phys. Rev. C **41**, 1147 (1990).

[2] T. Motobayashi *et al.*, Phys. Lett. B **346**, 9 (1995).

[3] E. Caurier, F. Nowacki, A. Poves, and J. Retamosa, Phys. Rev. C **58**, 2033 (1998).

[4] Y. Utsuno, T. Otsuka, T. Mizusaki, and M. Honma, Phys. Rev. C **60**, 054315 (1999).

[5] H. Iwasaki *et al.*, Phys. Lett. B **522**, 227 (2001).

[6] Y. Yanagisawa *et al.*, Phys. Lett. B **566**, 84 (2003).

[7] I. Tanihata *et al.*, Phys. Lett. B **289**, 261 (1992); I. Tanihata, J. Phys. G **22**, 157 (1996).

[8] A. S. Jensen *et al.*, Rev. Mod. Phys. **76**, 215 (2004).

[9] B. Jonson, Phys. Rep. **389**, 1 (2004).

[10] M. Takechi *et al.*, Nucl. Phys. A **834**, 412c (2010).

[11] T. Nakamura *et al.*, Phys. Rev. Lett. **103**, 262501 (2009).

[12] A. Gade *et al.*, Phys. Rev. C **77**, 044306 (2008).

[13] G. Bertsch, J. Borysowicz, H. McManus, and W. G. Love, Nucl. Phys. A **284**, 399 (1977).

[14] J.-P. Jeukenne, A. Lejeune, and C. Mahaux, Phys. Rev. C **16**, 80 (1977); Phys. Rep. **25**, 83 (1976).

[15] F. A. Brieva and J. R. Rook, Nucl. Phys. A **291**, 299 (1977); **291**, 317 (1977); **297**, 206 (1978).

[16] G. R. Satchler and W. G. Love, Phys. Rep. **55**, 183 (1979).

[17] G. R. Satchler, *Direct Nuclear Reactions* (Oxford University Press, Oxford, 1983).

[18] N. Yamaguchi, S. Nagata, and T. Matsuda, Prog. Theor. Phys. **70**, 459 (1983); **76**, 1289 (1986).

[19] L. Rikus, K. Nakano, and H. V. von Geramb, Nucl. Phys. A **414**, 413 (1984); L. Rikus and H. V. von Geramb, *ibid.* **426**, 496 (1984).

[20] K. Amos, P. J. Dortmans, H. V. von Geramb, S. Karataglidis, and J. Raynal, in *Advances in Nuclear Physics*, edited by J. W. Negele and E. Vogt (Plenum, New York, 2000), Vol. 25, p. 275.

[21] T. Furumoto, Y. Sakuragi, and Y. Yamamoto, Phys. Rev. C **78**, 044610 (2008); **79**, 011601(R) (2009); **80**, 044614 (2009).

[22] D. T. Khoa, W. von Oertzen, H. G. Bohlen, and S. Ohkubo, J. Phys. G **34**, 111R (2007).

[23] M. Yahiro, K. Ogata, and K. Minomo, Prog. Theor. Phys. **126**, 167 (2011).

[24] J. Terasaki, H. Flocard, P.-H. Heenen, and P. Bonche, Nucl. Phys. A **621**, 706 (1997).

[25] R. Rodríguez-Guzmán, J. L. Egido, and L. M. Robledo, Nucl. Phys. A **709**, 201 (2002).

[26] M. Yamagami and Nguyen Van Giai, Phys. Rev. C **69**, 034301 (2004).

[27] R. R. Rodríguez-Guzmán, J. L. Egido, and L. M. Robledo, Eur. Phys. J. A **17**, 37 (2003).

[28] M. Kimura and H. Horiuchi, Prog. Theor. Phys. **111**, 841 (2004).

[29] M. Kimura, Phys. Rev. C **75**, 041302(R) (2007).

[30] K. Minomo, T. Sumi, M. Kimura, K. Ogata, Y. R. Shimizu, and M. Yahiro, Phys. Rev. C **84**, 034602 (2011).

[31] K. Minomo, T. Sumi, M. Kimura, K. Ogata, Y. R. Shimizu, and M. Yahiro, Phys. Rev. Lett. **108**, 052503 (2012).

[32] R. Wyss (private communication) (2005).

[33] K. M. Watson, Phys. Rev. **89**, 575 (1953).

[34] A. K. Kerman, H. McManus, and R. M. Thaler, Ann. Phys. (NY) **8**, 551 (1959).

[35] M. Yahiro, K. Minomo, K. Ogata, and M. Kawai, Prog. Theor. Phys. **120**, 767 (2008).

[36] B. Sinha, Phys. Rep. **20**, 1 (1975); B. Sinha and S. A. Moszkowski, Phys. Lett. B **81**, 289 (1979).

[37] T. Furumoto, Y. Sakuragi, and Y. Yamamoto, Phys. Rev. C **82**, 044612 (2010).

[38] K. Minomo, K. Ogata, M. Kohno, Y. R. Shimizu, and M. Yahiro, J. Phys. G **37**, 085011 (2010).

[39] R. Machleidt, K. Holinde, and Ch. Elster, Phys. Rep. **149**, 1 (1987).

[40] J. F. Berger, M. Girod, and D. Gogny, Comput. Phys. Commun. **63**, 365 (1991).

[41] W. Nazarewicz and P. Rozmej, Nucl. Phys. A **369**, 396 (1981).

[42] T. Shoji and Y. R. Shimizu, Prog. Theor. Phys. **121**, 319 (2009).

[43] S. Cwiok, J. Dudek, W. Nazarewicz, J. Skalski, and T. Werner, Comput. Phys. Commun. **46**, 379 (1987).

[44] V. M. Strutinsky, Nucl. Phys. A **122**, 1 (1968).

[45] M. Brack, J. Damgård, A. S. Jensen, H. C. Pauli, V. M. Strutinsky, and C. Y. Wong, Rev. Mod. Phys. **44**, 320 (1972).

[46] W. D. Myers and W. J. Swiatecki, Nucl. Phys. **81**(1), 1 (1966); **81**(2), 1 (1966); Ark. Phys. **36**, 343 (1967).

[47] N. Tajima, Y. R. Shimizu, and S. Takahara, Phys. Rev. C **82**, 034316 (2010).

[48] P. Ring and P. Schuck, *The Nuclear Many-Body Problem* (Springer, New York, 1980).

[49] T. Ono, Y. R. Shimizu, N. Tajima, and S. Takahara, Phys. Rev. C **82**, 034310 (2010).

[50] S. Tagami and Y. R. Shimizu, Prog. Theor. Phys. **127**, 79 (2012).

[51] L. J. Tassie and F. C. Barker, Phys. Rev. **111**, 940 (1958).

[52] W. Horiuchi, Y. Suzuki, B. Abu-Ibrahim, and A. Kohama, Phys. Rev. C **75**, 044607 (2007).

[53] M. Takechi *et al.*, Phys. Rev. C **79**, 061601(R) (2009).

[54] L. Chulkov *et al.*, Nucl. Phys. A **603**, 219 (1996).

[55] T. Suzuki *et al.*, Phys. Rev. Lett. **75**, 3241 (1995).

[56] H. de Vries, C. W. de Jager, and C. de Vries, At. Data Nucl. Data Tables **36**, 495 (1987).

[57] R. P. Singhal *et al.*, Nucl. Instrum. Methods **148**, 113 (1978).

[58] W. G. Love and M. A. Franey, Phys. Rev. C **24**, 1073 (1981); **31**, 488 (1985).

[59] M. Lacombe, B. Loiseau, J. M. Richard, R. VinhMau, J. Conte, P. Pires, and R. deTourreil, Phys. Rev. C **21**, 861 (1980).

[60] T. Ichihara *et al.*, Nucl. Phys. A **569**, 287c (1994).

[61] R. G. Stokstad *et al.*, Phys. Rev. C **20**, 655 (1979).

[62] [http://www.nndc.bnl.gov/chart].

[63] B. Jurado *et al.*, Phys. Lett. B **649**, 43 (2007).

[64] G. Audi, A. H. Wapstra, and C. Thibault, Nucl. Phys. A **729**, 337 (2003).

[65] M. Kamimura, M. Yahiro, Y. Iseri, Y. Sakuragi, H. Kameyama, and M. Kawai, Prog. Theor. Phys. Suppl. **89**, 1 (1986).

[66] N. Austern, Y. Iseri, M. Kamimura, M. Kawai, G. Rawitscher, and M. Yahiro, Phys. Rep. **154**, 125 (1987).

[67] N. Austern, M. Yahiro, and M. Kawai, Phys. Rev. Lett. **63**, 2649 (1989).

[68] N. Austern, M. Kawai, and M. Yahiro, Phys. Rev. C **53**, 314 (1996).

[69] A. Deltuva, A. M. Moro, E. Cravo, F. M. Nunes, and A. C. Fonseca, Phys. Rev. C **76**, 064602 (2007).

[70] K. Rusek and K. W. Kemper, Phys. Rev. C **61**, 034608 (2000).

[71] J. A. Tostevin, F. M. Nunes, and I. J. Thompson, Phys. Rev. C **63**, 024617 (2001).

[72] B. Davids, S. M. Austin, D. Bazin, H. Esbensen, B. M. Sherrill, I. J. Thompson, and J. A. Tostevin, Phys. Rev. C **63**, 065806 (2001).

[73] J. Mortimer, I. J. Thompson, and J. A. Tostevin, Phys. Rev. C **65**, 064619 (2002).

[74] K. Ogata, M. Yahiro, Y. Iseri, T. Matsumoto, and M. Kamimura, Phys. Rev. C **68**, 064609 (2003).

[75] T. Matsumoto, E. Hiyama, K. Ogata, Y. Iseri, M. Kamimura, S. Chiba, and M. Yahiro, Phys. Rev. C **70**, 061601(R) (2004).

[76] D. J. Howell, J. A. Tostevin, and J. S. Al-Khalili, J. Phys. G: Nucl. Part. Phys. **31**, S1881 (2005).

[77] K. Rusek, I. Martel, J. Gómez-Camacho, A. M. Moro, and R. Raabe, Phys. Rev. C **72**, 037603 (2005).

[78] T. Matsumoto, T. Egami, K. Ogata, Y. Iseri, M. Kamimura, and M. Yahiro, Phys. Rev. C **73**, 051602(R) (2006).

[79] A. M. Moro, K. Rusek, J. M. Arias, J. Gómez-Camacho, and M. Rodríguez-Gallardo, Phys. Rev. C **75**, 064607 (2007).

[80] M. Rodríguez-Gallardo, J. M. Arias, J. Gómez-Camacho, R. C. Johnson, A. M. Moro, I. J. Thompson, and J. A. Tostevin, Phys. Rev. C **77**, 064609 (2008).

[81] M. Rodríguez-Gallardo, J. M. Arias, J. Gómez-Camacho, A. M. Moro, I. J. Thompson, and J. A. Tostevin, Phys. Rev. C **80**, 051601(R) (2009).

[82] T. Matsumoto, K. Kato, and M. Yahiro, Phys. Rev. C **82**, 051602(R) (2010).

[83] M. Avrigeanu and A. M. Moro, Phys. Rev. C **82**, 037601 (2010).

[84] W. Horiuchi, Y. Suzuki, P. Capel, and D. Baye, Phys. Rev. C **81**, 024606 (2010).

[85] H. S. Than, D. T. Khoa, and N. V. Giai, Phys. Rev. C **80**, 064312 (2009).

[86] D. T. Loan, N. H. Tan, D. T. Khoa, and J. Margueron, Phys. Rev. C **83**, 065809 (2011).

[87] F. Chappert, M. Girod, and S. Hilaire, Phys. Lett. B **668**, 420 (2008).

[88] W. Satula, J. Dobaczewski, and W. Nazarewicz, Phys. Rev. Lett. **81**, 3599 (1998).

[89] T. Otsuka, T. Matsuo, and D. Abe, Phys. Rev. Lett. **97**, 162501 (2006).

[90] S. Hilaire and M. Girod, Eur. Phys. J. A **33**, 237 (2007).

[91] [http://www-phynu.cea.fr/science_en_ligne/carte_potentiels _microscopiques/carte_potentiel_nucleaire_eng.htm].

[92] K. Bennaceur, J. Dobaczewski, and M. Ploszajczak, Phys. Lett. B **496**, 154 (2000).

[93] K. Hagino and H. Sagawa, Phys. Rev. C **84**, 011303(R) (2011).